INVESTIGATION OF TITANIUM-MANGANESE-VANADIUM ELECTROLYTES AS CATHOLYTE FOR DUAL-CIRCUIT REDOX FLOW BATTERIES

A Thesis submitted to

Indian Institute of Science Education and Research Pune

in partial fulfilment of the requirements for the

BS-MS Dual Degree Programme

By

Mr. Vimanshu Chanda

Registration Number: 20141122

Supervisor: Prof. Hubert H. Girault

Professor, Institute of Chemical Sciences and Engineering (ISIC)

École Polytechnique Fédérale de Lausanne, Valais Wallis.

Rue de l'Industrie 17, Case postale 440,
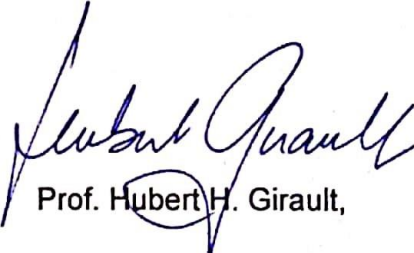
CH-1950 Sion, Switzerland

Certificate

This is to certify that this dissertation entitled "**Investigation of Titanium-Manganese-Vanadium electrolytes as Catholyte for dual circuit redox flow batteries**" towards the partial fulfilment of the BS-MS dual degree programme at the **Indian Institute of Science Education and Research, Pune** represents study/work carried out by **Vimanshu Chanda (Reg. No. 20141122)** at **École polytechnique fédérale de Lausanne, Sion, Switzerland** under the supervision of **Prof. Hubert H. Girault, Director (Laboratoire d' Electrochimie Physique et Analytique) during the academic year 2018/2019.**

Date: 28/04/2019

Place: Switzerland

Sion

Prof. Hubert H. Girault,

Director, LEPA

EPFL Valais Wallis, Switzerland

Declaration

I hereby declare that the matter embodied in the report entitled **Investigation of Titanium-Manganese-Vanadium electrolytes as Catholyte for dual circuit redox flow batteries** are the results of the work carried out by me at EPFL Valais Wallis, LEPA, Switzerland under the supervision of Prof. Hubert H. Girault and the same has not been submitted elsewhere for any other degree.

Date: 26/02/2019

Place: Switzerland

Vimanshu Chanda

(Reg. No.20141122)

Acknowledgements

I wish to express my sincere everlasting gratitude to my supervisor *Professor Hubert Girault* for giving me this stupendous opportunity of doing the thesis project with him. I would like to thank him for his guidance, valuable suggestions, cooperation, affection and his trust in me throughout this project. It was an honor to work under his guidance, not only because of his unbound patience but also an extremely generous assistance.

I would like to thank my supervisor in India *Dr. Muhammed Musthafa O. T.,* Assistant Professor, Department of Chemistry, IISER Pune for his guidance throughout my research journey at IISER Pune.

I take this opportunity to express my heartfelt gratitude to *Dr. Solène Gentil* for her support and guidance throughout the project and providing valuable suggestions and comments for my thesis that certainly improved it significantly. Also, I would like to sincerely thank *Dr. Pekka Peljo* for his guidance and sharing the precocious time and valuable hands-on experience throughout the project.

I would like to thank with a special mention to *Sunny Maye* (PhD student) and *Danick Reynard* (PhD student) for performing the experiments with me, reading my thesis and giving necessary guidance and advices throughout the project making life easier. I choose this moment to acknowledge the contribution greatly.

I express my sincere gratitude to all my lab mates for their encouragement, valuable time, and co-operation throughout the duration of my project. I would also like to say a big thank you to *Madame Patricia Byron* for her unconditional smile and continuous help in administrative works during my stay.

Finally, I want to thank my parents, brother & sister who have always supported me and appreciated my work wholeheartedly and been my inspiration.

Table of Content

List of Abbreviations

RFB: redox flow batteries

GC: glassy carbon electrode

List of Figures

List of Tables

ABSTRACT

Dual circuit redox flow battery (RFB) serves as a viable means to bypass the low energy density of conventional flow batteries converting stored power to gas in the form of hydrogen and oxygen. It was previously studied by Amstutz *et al* for a vanadium - cerium RFB which suffered from degradation due to the high oxidizing properties of cerium electrolyte. The present master thesis focuses on utilizing manganese as a positive electrolyte thereby proposing an alternative to the V-Ce system. Mn(II)/Mn(III) redox potential is 1.51 V *vs.* SHE and could therefore be suitable for oxygen evolution reaction. However, Mn(III) is known for its disproportionation at high potentials (>1.6V *vs.* SHE), leading to the formation of MnO_2 solid particles and Mn^{2+}. Therefore, in order to prevent the disproportionation, TiO^{2+} and VO_2^+ were used as additives. As a perspective, a dual V-Mn-Ti system was investigated. The electrochemical behavior of Mn(II)/Mn(III) couple along with the addition of TiO_2^+ and VO_2^+ ions was thoroughly investigated using cyclic voltammetry, rotating disk and rotating-ring disk electrode. It was shown that the disproportionation reaction of Mn(III) cannot be totally restrained with the addition of TiO_2^+ or VO_2^+. The extent of MnO_2 plating reduced on carbon felt electrodes was notably observed to quite an extent with the presence of Ti(IV) and V(V), which was further confirmed by SEM. It was shown that 1:1:1 of Ti/V/Mn in 5M H_2SO_4 was the best compromise to reduce the formation of $MnO_2(s)$. Further, a H-cell test to chemically discharge Mn(III) on IrO_2 catalyst was performed for the purpose of oxygen evolution reaction. However, it resulted in low efficiency towards oxygen evolution owing to the disproportionation of Mn(III).

Chapter 1. Introduction

The excessive use of non-renewable sources of energy is causing them to deplete at a faster rate than expected. Combustion of these non-renewable resources causes the emission of harmful gases due to which 21st century is facing the problem of paramount pollution and anthropogenic global warming [1]. Exhausting fuel reservoirs and increasing environmental pollution drives people to find alternative sources of energy. Various large-scale energy storage systems have been developed such as pumped hydro and compressed air systems but they have geographical limitations [1-2]. Electrochemical energy storage devices (EESD) acts as an imperative source for storing energy and can be released and used whenever needed, providing an alternative solution to the issues of power generation and consumption. Over the last few decades, the need for energy storage devices and their utilization in power systems have been a reason for concern. Their role in various hybrid automobiles and renewable energy generation is of wide importance Batteries, fuel cells and super capacitors can efficiently store energy and can be considered as reliable EESDs [1-3].

1.1 <u>Battery:</u>

A battery converts chemical energy directly into electric energy by means of electro-chemical reaction. It has two half-cells, consisting of a cathode (positive electrode) and an anode (negative electrode). The electrochemical reaction occurs at the electrode/electrolyte interface, thereby creating a potential difference. Due to this, migration of electrons take place from region of low to high reduction potentials, subsequently converting the chemical energy to electrical energy [3-4]. They can be classified into two types: primary and secondary batteries. A primary cell can be used only once as chemical reaction undergoing in the cell is not reversible so supply of reactants will cease with time, which cannot be regenerated making it unrechargeable [5]. Common examples are the alkaline batteries, Zinc-Carbon and Aluminium-air battery. A secondary cell can be charged and reused multiple times, as the chemical reaction undergoing in the cell can be reversed by applying current to it [5]. *eg.* lead acid, Nickel-Cadmium and Lithium-ion battery.
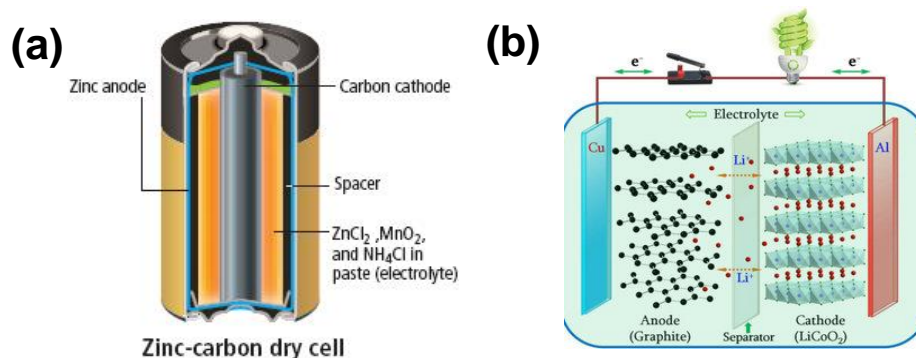
Figure 1.1: Schematic of (a) Zinc-Carbon battery [6] (b) Li-ion battery [7]

Li-ion batteries have been the most widely and rigorously used battery in applications ranging from portable devices such as smart phones to hybrid electric vehicles owing to its very high energy density of 100-250 Wh kg^{-1}. The anode utilizes a graphite electrode whereas an intercalating cathode made up of $LiCoO_2$ / $LiMn_2O_4$ /$LiFePO_4$ is used. Electrolytes based on lithium salts ($LiPF_6$, $LiBF_4$, $LiClO_4$) are used with organic solvents such as ethylene / dimethyl carbonate. The main limitation includes lithium dendrite formation with high packaging cost [8-9]. Further, Nickel based battery employs nickel hydroxide as the positive electrode material with cadmium, metal hydride or zinc as the negative electrode. It demonstrates moderate charge-discharge efficiency (70-90%) with relatively low specific energy density (40-80 Wh kg^{-1}). The hazardous nature and high cost of cadmium limits its trade off [9-10]. Over the past few decades, metal air batteries have attracted much attention as a possible alternative energy storage device for Li-ion due to the high theoretical energy density and the low cost of metal component (Li, Zn, Al, Mg, Na and K). They are promising for future generation electric vehicles since they use oxygen from air as one of the reactants reducing the weight of the battery. Zn-air batteries have received considerable attention as it is relatively stable in both aqueous and alkaline electrolytes and due to its high theoretical specific energy density (1084 Wh kg^{-1}) [9, 11]. Metal sulfur systems particularly include lithium and sodium sulfur batteries. They are quite popular due to their high specific energy density (60-120 Wh kg^{-1}). In these batteries lithium/molten sodium are present at the anode while molten sulfur is used at cathode owing to its high abundance, electrochemical properties and low cost. However, the major problem for metal sulfur batteries is its rapid capacity fading and low conductivity of sulfur, which is mainly due to dissolution of polysulphide anions (S_n^{2-})-intermediate reaction species formed on charge and discharge from the cathode into the electrolyte [9, 12]. Figure 1.2 illustrates

a comparison profile displaying energy densities for the different batteries mentioned above.
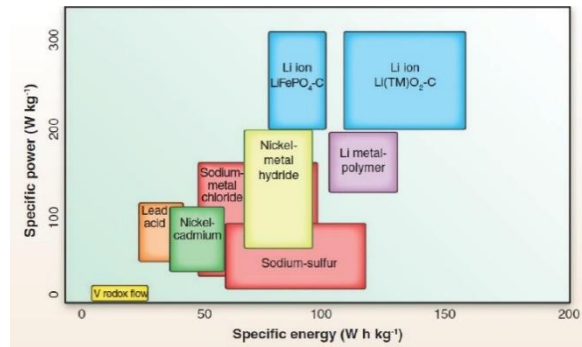
Figure 1.2: Ragone plot of most common batteries used for large-scale energy storage [13]

1.2 Redox Flow battery - State of the art:

In the early seventies, the National Aeronautics and Space Administration (NASA), as a first, developed the concept of redox flow batteries[14], derived from redox fuel cells, published by Posner and co-workers in 1955[15].They were based on two electrolytes, which were flowed through the positive and negative chambers respectively, containing two electrodes where the electroactive species reacted. An ion-exchange membrane or a ceramic membrane was used to separate the two chambers. The two electrodes were connected through an external circuit sanctioning the use of generated electricity, thereby powering an electric load. The electrolytes were discharged onto the electrode generating a current, followed by the regeneration of electrolytes alongside, via chemically or electrochemically [15-16].

Similarly, the principle of redox flow batteries is also governed via employing two electrolytes, which are made to flow through a central electrochemical cell, but on the contrary, as compared to redox fuel cells, the electrolytes can be regenerated again through the reverse reaction at the electrode, behaving in the same way as conventional rechargeable batteries. Generally, RFB systems utilizes aqueous based electrolytes, which are responsible for the transportation of water soluble redox species. A strong acid (or in some cases, a strong base) is used as a supporting electrolyte in RFBs, while some systems even utilize additives thereby enhancing the solubility of redox active species. The electrolytes, stored in tanks, circulate in each of the half-cell carrel where the electrochemical reactions take place[17-18].

The unique configuration and operation of RFBs is attributed to decoupled energy storage and power generation. In fact, we can increase the capacity of these batteries by increasing the size of the tanks while the power can be tuned with the amount of electrode surface available. The major advantages of flow batteries include minimal response time, large-scale durability, low self-discharge [8, 18-20]. The main limitation of RFBs resides in their low energy density (25-30 Wh kg^{-1}). (Figure 1.2) [13].
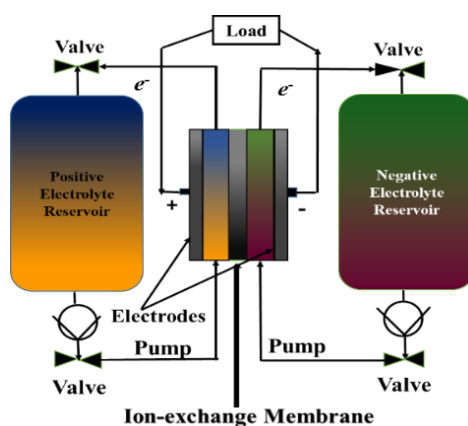
Figure 1.3: General Scheme of a redox flow battery.

1.3 <u>RFB Components</u>:

The two main components of RFBs include electrodes and membranes. Since the development of redox flow batteries until now, researchers throughout the world have significantly utilized electrodes based on carbon material such as carbon rods, felt, graphite cloth, foam and chips[21-23]. Materials such as silver, silver chloride, mercury, mercurous-silver, tungsten-rhenium, lead, bismuth, gold, platinum, platinized titanium were also tested[21]. Three-dimensional carbon materials with the likes of carbon felt[23] and reticulated vitreous carbon[24] have been utilized more often owing to their large volumetric surface area, typically ranging between 240-400 cm^2 cm^{-3} and 5-70 cm^2 cm^{-3} respectively. They demonstrates decent electrochemical activity, has a wide potential window with low degradation with number of cycles.

Major criteria concerning the choice of electrode materials in a RFB should be a porous electronic conductor, electrochemically inert whilst displaying good chemical and mechanical stability. Skyllas *et al* [25] tried to incorporate metals (Pt^{4+}, Pd^{2+}, Te^{4+}, Mn^{2+}, Ir^{3+}, Au^{4+}), via treatment with ion exchange solutions, on carbon and graphite felt electrodes in order to enhance their conductivity and catalytic properties. Li *et al* [26]

mentioned a novel way to modify the carbon felt utilizing multi walled carbon nanotubes, thereby increasing the electrochemical activity and reversibility of the vanadium redox couples.

As shown in Figure 1.3, a separator is required in a RFB acting as a physical barrier, thus avoiding the cross mixing of both anolytes and catholyte. Ion exchange membrane (IEM) is utilized as separators, processed through polymeric materials with a pore diameter thickness of 20 Å [27]. IEM can be classified in two, *i.e.* anion exchange and cation exchange used to conduct negatively charged (*i.e.* Cl^-, NO_3^-, SO_4^{2-}) and positively charged ions (*i.e.* H^+ or Na^+) respectively. An ideal candidate for the membrane should possess high chemical and mechanical stability for a long lifetime. These factors are decisive in RFBs as highly oxidizing electrolytes are used leading to the degradation of membrane. Further, it is desirable to have an excellent ion conductivity, vital for the transfer of ions therefore curtailing the ohmic drop losses, effecting the voltage efficiency of a battery. Ion selectivity is also imperative for the selection of the membrane, avoiding cross mixing of the species, leading to self-discharge decreasing the efficiency of the RFB [27-29].

Cation exchange membranes, the prevalent ones, are classified based on different chemical composition, *i.e.* perfluorinated, partially fluorinated, and non-fluorinated[30]. Nafion membrane due to its excellent thermal and mechanical stability along with its high proton conductivity is the most used membrane in the context of RFBs. It was prepared through incorporation of perfluorovinyl ether groups on a polytetrafluoroethylene (PTFE, or Teflon) polymer, with edges of former terminating on sulfonate groups. The limiting factor considering the Nafion N117 membrane is the permeability of the cations, which is approximately $30 \cdot 10^{-7}$ cm^2 min^{-1} for V(IV) ions in an all vanadium RFBs [30-31] .

Anion exchange membranes are preferred to circumvent the cross mixing of cations thereby allowing the movement of anions from one side to another. Although it is still limited by the proton conduction, poor chemical stability and water transport [32].

Amphoteric ion-exchange membranes contains both cationic and anionic functional moieties, thereby promoting ion selectivity. Recently, Quia *et al* developed a novel strategy to modify nafion N117 membrane using a layer by layer self-assembly

technique utilizing polycations poly(diallyldimethylammonium chloride) and polyanions poly(sodium styrene sulfonate) layers achieving proton conductivity (*i.e.* 0.048 S cm^{-1}) comparable to commercially available nafion N117 (*i.e.* 0.058 S cm^{-1}) [33].

1.3 <u>RFB chemistries:</u>

Over the last 40 years, numerous redox couples have been investigated in order to scale up the overall performance. The redox potential and solubility of the redox species is the main criterion dictating the overall energy density of the battery. Increasing the solubility of a particular redox species yields in higher energy density. Reversibility of the active species in each half-cell is necessary to facilitate electron transfer Moreover, the active species should be stable in the operating potential window. Table 1 and 2 illustrates the various cathodic and anodic redox couples used by far with an emphasis on transition metal ions.

Redox couples	E^O [V vs. SHE]	Reaction	References
V^{3+} / V^{2+}	- 0.26	$V^{3+} + 1e^- \rightleftharpoons V^{2+}$	34
Fe^{2+} / Fe	-0.3	$Fe^{2+} + 2e^- \rightleftharpoons Fe$	35
Pb^{2+} / Pb	-0.13	$Pb^{2+} + 2e^- \rightleftharpoons Pb$	19
Zn^{2+} / Zn	-0.76	$Zn^{2+} + 2e^- \rightleftharpoons Zn$	35
Cr^{3+} / Cr^{2+}	-0.41	$Cr^{3+} + 1e^- \rightleftharpoons Cr^{2+}$	35
S_4^{2-} / S_2^{2-}	-0.26	$S_4^{2-} + 2e^- \rightleftharpoons S_2^{2-}$	19

Table 1: Cathodic redox couples used in RFB.

Redox couples	E^O [V vs. SHE]	Reaction	References
Ce^{4+} / Ce^{3+}	+ 1.75	$Ce^{4+} + 1e^- \rightleftharpoons Ce^{3+}$	36
Fe^{3+} / Fe^{2+}	+ 0.77	$Fe^{3+} + 1e^- \rightleftharpoons Fe^{2+}$	35
Br^{3-} / Br^-	+ 1.09	$Br_3^- + 2e^- \rightleftharpoons 3Br^-$	35
PbO_2 / Pb^{2+}	+ 1.49	$PbO_2 + 4H^+ + 2e^- \rightleftharpoons Pb^{2+} + 2H_2O$	35
VO_2^+ / VO^{2+}	+ 1.00	$VO_2^+ + 2H^+ + 1e^- \rightleftharpoons VO^{2+} + 2H_2O$	34
Mn^{3+} / Mn^{2+}	+ 1.51	$Mn^{3+} + 1e^- \rightleftharpoons Mn^{2+}$	37

Table 2: Anodic redox couples used in RFB.

RFB system (liquid phase)	Redox couple	ΔE^O [V]	Electrodes	Membrane	Electrolytes	Ref.
All vanadium	+ = VO^{2+}/VO_2^+ - = V^{3+} / V^{2+}	1.26	Carbon/graphite felt	Nafion	2M H_2SO_4	34

System	Redox couples	Voltage	Electrode	Membrane	Electrolyte	Ref
Iron-Chromium	+ = Fe^{3+} / Fe^{2+} - = Cr^{3+} / Cr^{2+}	1.18	Carbon felt	CEM	HCl in H_2O	36
Zinc-Cerium	+ = Ce^{4+} / Ce^{3+} - = Zn^{2+}/ Zn	2.4	Carbon/Ti mesh	Nafion	MSA	42
Vanadium-Cerium	+ = Ce^{4+} / Ce^{3+} - = V^{3+} / V^{2+}	1.93	Carbon/graphite felt		1-2M H_2SO_4	34
Bromine - Polysulphide	+ = Br_3^- / Br - = S_4^{2-} / S_2^{2-}	1.36	Activated carbon	CEM	H_2O	38
Vanadium Polyhalide	+ = $BrCl_2^-$ / Cl^- - = V^{3+} / V^{2+}	1.36	Graphite felt	Nafion	1.5M HCl in H_2O	43
Vanadium-manganese	+ = Mn^{3+} / Mn^{2+} - = V^{3+} / V^{2+}	1.77	Carbon/graphite felt	Nafion/AEM	5M H_2SO_4 in H_2O	37

Table 3: Characteristics all liquid phase RFB systems

RFB systems operating with more than one redox couples have been reported recently. This is of particular interest as it reduces the effect of cross mixing and further increases the energy density of the overall system. Wang *et al* [44] reported a hybrid Fe/V RFB operated on mixed electrolyte combination of both the species. On the negative side, only V^{3+}/ V^{2+} was used whereas on the positive side both VO_2^+/ VO^{2+} along with Fe^{3+}/ Fe^{2+} was placed, achieving stable performances.
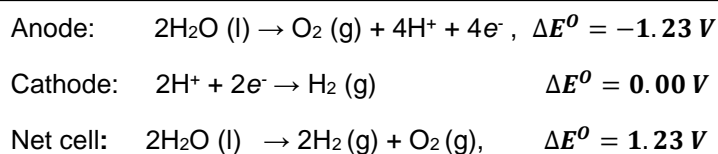
1.4 <u>Applications:</u>

In essence, RFBs serves as an imperative source and technology for energy storage and electric vehicle applications. It displays certain advantages in comparison to conventional rechargeable batteries owing to its modular design, scalability, flexible operation and maintenance cost. RFBs acts as a promising candidate for stationary applications related to peak shaving, load levelling and acting as a power supply unit in remote areas, possessing no geographical limitations. Moreover, their output power is independent of the storage capacity allowing better flexibility of the system. Moreover, technological advancements have been carried out for RFBs allowing it to withstand the intermittent behaviour of solar or wind production. From the last five decades, the flow battery technology has diversified and has made significant advances, but still a very few systems have been tested on large scale demonstrating stable performances. To further improve the RFB system with respect to the grid scale energy storage and mobile applications, optimization of the setup is very important regarding the flow geometries, the state of charge sensors etc. Notably, attention towards the development of low cost electrode materials and membrane assemblies is required to scale up the commercialization [17-20].
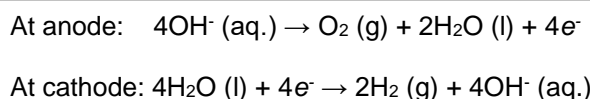
Chapter 2. Water Electrolysis
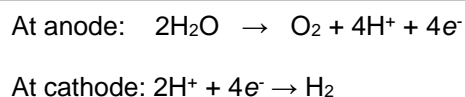
2.1 <u>Water Electrolysis:</u>

Generally, water electrolysis refers to the splitting of a water molecule into hydrogen (H_2) and oxygen (O_2), via applying a potential between the two electrodes of an electrochemical cell. The standard potential between these two half-cell reactions is 1.23 V *vs.* SHE. However, in majority of the cases, a higher potential is enforced than the standard thermodynamic potential owing to kinetic and mass transfer factors, termed as overpotential. Ideally, the electrodes should exhibit following properties *i.e.* corrosion resistant, good electronic conductivity and catalytic properties[45-46]. The reaction will proceed with low overpotential on platinum electrode as compared to carbon / graphite electrodes owing to the catalytic activity of platinum[47]. It can be achieved in alkaline and acidic medium, while possessing limited capability in neutral conditions. The corresponding reaction for hydrogen evolution (HER) and oxygen evolution reaction (OER) are:

Anode: $2H_2O$ (l) → O_2 (g) + $4H^+$ + $4e^-$, $\Delta E^O = -1.23\ V$

Cathode: $2H^+ + 2e^- → H_2$ (g) $\Delta E^O = 0.00\ V$

Net cell: $2H_2O$ (l) → $2H_2$ (g) + O_2 (g), $\Delta E^O = 1.23\ V$

In alkaline conditions

At anode: $4OH^-$ (aq.) → O_2 (g) + $2H_2O$ (l) + $4e^-$

At cathode: $4H_2O$ (l) + $4e^-$ → $2H_2$ (g) + $4OH^-$ (aq.)

In acidic conditions

At anode: $2H_2O$ → O_2 + $4H^+$ + $4e^-$

At cathode: $2H^+ + 4e^- → H_2$

2.2 <u>Catalysts for OER:</u>

Water oxidation is one of the most complex reactions in electrochemistry, involving the transfer of four electrons and four protons and kinetic limitations associated with the formation intermediates, overcoming a huge energy barrier. In electrochemical water oxidation, the two factors governing the reaction is the voltage applied, along with the catalyst required to accelerate the reaction. Over the last decades, research is ongoing in order to develop novel electrocatalyst required for the oxidation of water, achieving less overpotential [45-47]. There has been very few reports regarding the water oxidation in acidic medium as most of the catalysts studied and investigated in the literature is

in alkaline conditions. IrO_2 and RuO_2 are considered as the best catalyst for water oxidation in both acidic and alkaline medium owing to their high activity and stability [45, 48]. However, corrosion issues with RuO_2 makes it less efficient to utilize widely. As both Ir and Ru are noble metals and highly expensive, significant efforts have been made by researchers in order to develop alternatives for the aforementioned. During the last few years, the focus is been on transitional metal oxides and perovskite materials[49] as they display comparable stability and electrocatalytic activity. Trotochaud et al [50] suggested the use of transitional metal based catalysts for water oxidation emphasizing specifically on Mn, Ru, Ir, and Fe. Morita [51] and co-workers studied manganese oxide mixed with electrocatalytically active RuO_2 as catalyst for OER and reported a relatively high activity for the anodic evolution of oxygen with the mixed oxide of MnO_2 and Mn_2O_3 as compared with the pure MnO_2.

2.3 <u>Dual-Circuit redox flow battery for indirect water electrolysis:</u>

To overcome the low energy density of conventional RFBs, Amstutz and co-workers[52-53] introduced a novel concept by enumerating a secondary level of energy storage to a RFB. The secondary circuit has the advantage of converting stored electrochemical energy in the batteries in the form of hydrogen and oxygen, demonstrating indirect water electrolysis. This includes a second pathway to discharge chemically the RFB, allowing the system to generate hydrogen and oxygen using catalytic beds as heterogeneous catalyst, without affecting the functioning of the RFB. It increases the capacity of the system with no significant increase in its volume, thereby achieving higher volumetric energy density than conventional flow batteries. The concept of dual-circuit redox flow battery was studied for a V-Ce RFB (Figure 2.1). V(II)/V(III) redox couple with a redox potential of -0.25 V *vs.* SHE was utilized on the negative side serving as a mediator for hydrogen evolution reaction. Ce(III)/Ce(IV) with a high redox potential of +1.75 V *vs.* SHE was employed for the purpose of OER. During the charging process, Ce(III) undergoes oxidation to Ce(IV), whereas V(III) reduces to V(II). Upon discharge, the reverse reactions occur.

<div style="border:1px solid black; padding:10px;">

Electro-chemical Reaction:

Positive side: $Ce^{3+} \rightleftharpoons Ce^{4+} + e^-$ E^o = +1.72 V *vs.* SHE

Negative side: $V^{3+} + e^- \rightleftharpoons V^{2+}$ E^o = -0.26 V vs. SHE

</div>
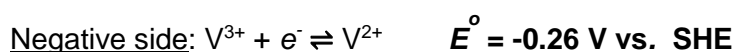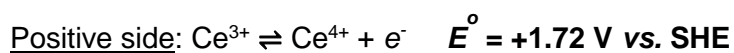
Upon demand the charged electrolytes can be passed through so-called "secondary circuits" to be discharged onto the heterogeneous catalytic beds evolving hydrogen and oxygen according to the following equations mentioned below. As both the reaction proceeds via multi electron and proton steps, a catalyst is required to accelerate the reaction.

Ce(IV) is chemically discharged through the oxidation of water to oxygen on RuO_2 catalyst whereas V(II) is chemically discharged through proton reduction to hydrogen on Mo_2C catalyst. The HER and OER catalytic efficiencies were around 96% and 78% respectively. The overall energy efficiency of the system as reported by the authors were 50% (i.e. the energy required to fully charge the battery with respect to the production of hydrogen). The dual circuit flow configuration is exclusive serving both the factors, *i.e.* renewable energy storage along with the renewable conversion of power to gas.
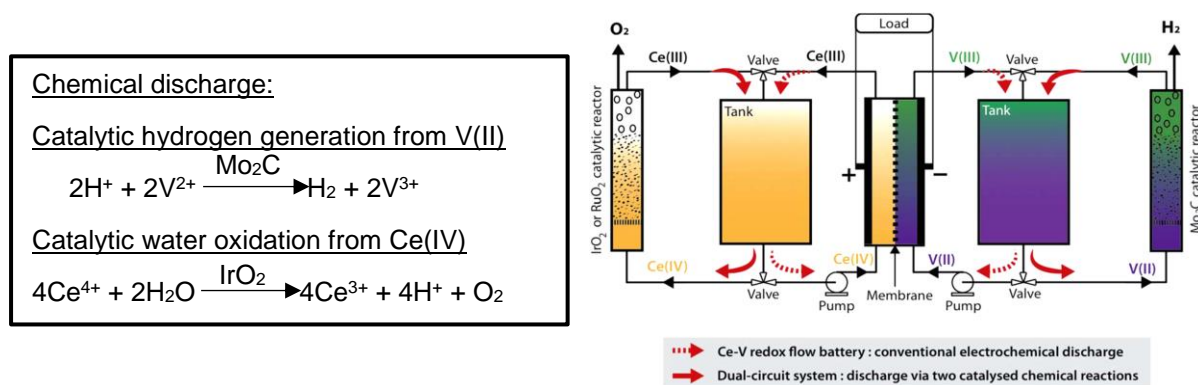

Figure 2.1 (a) Catalytic reactions for HER and OER (b) General scheme of a dual-circuit RFB, based on a V–Ce RFB [52]

However, the V-Ce indeed has some limitations: (i) The positive half-cell of V-Ce RFB suffered from degradation due to the high oxidizing properties of cerium electrolyte, leading to the corrosion of electrode materials, current collectors etc. (ii) cross mixing of V and Ce species decreases the capacity retention of the battery.

Objectives of the Master Thesis:

The objective of the present work was to investigate Mn(II)/Mn(III) redox couple as a positive active material providing an alternative to the above mentioned V-Ce system. Mn(II)/Mn(III) was thought to be used due to its high redox potential of 1.51 V *vs.* SHE [37].

2.4 Mn(II)/Mn(III) redox chemistry:

Mn(II)/Mn(III) redox couple is considered as a positive active material due to its high solubility and high redox potential of 1.51 V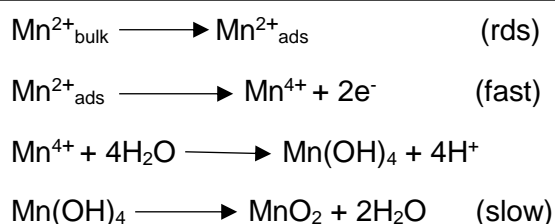 *vs.* SHE, comparable to vanadium ions. The main issue concerning the use of Mn redox couple is the chemically unstable nature of Mn(III), which disproportionate to form solid oxide particles of MnO_2(s) along with Mn(II). It was previously reported that Mn(III) can be stabilized by increasing the concentration of acid. However, this method was not significant as the energy density of Mn(III) system was still low [37, 54]. Different mechanisms have been proposed in the literature regarding the oxidation product of Mn(II), emphasizing on its electrodeposition. Fleischmann *et al* [55] studied the electrodeposition of Mn via applying constant potential, suggesting a three dimensional growth of MnO_2. The surface adsorbed ($Mn(II)_{ads}$) either oxidizes to $Mn(III)_{ads}$ or $Mn(IV)_{ads}$ with the former disproportioning to produce Mn(II) and MnO_2. Kao *et al* [56] investigated the electrodeposition of MnO_2 using a Pt RRDE and reported a three step mechanism with regard to the nature of Mn(II) oxidation product. They propose the electrochemical oxidation of Mn(II) to intermediates of Mn(III) subsequently getting adsorbed on the electrode. The nucleation and growth of MnO_2 occurs via the reduction of MnO_2 surfaces by Mn(II) ions in the solution giving rise to MnOOH. This is followed by the oxidation of these solid intermediates to form MnO_2(s) which was considered to be rate determining step.

$$Mn^{2+} \longrightarrow Mn^{3+} + e^-$$
$$Mn^{3+} + 2H_2O \longrightarrow MnOOH + 3H^+$$
$$MnOOH \longrightarrow MnO_2 + H^+ + e^-$$
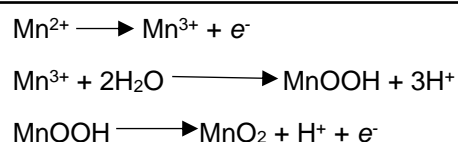
Paul and Cartwright [57-58] studied the electrodeposition of manganese using RDE and electrochemical impedance spectroscopy and suggested the diffusion of Mn(II) from bulk at the electrode surface to be rate determining step. The authors suggest a direct oxidation of Mn(II) to Mn(IV), preceding with formation of porous intermediates to (Mn_2O_3 or $Mn(OH)_4$), with subsequent hydrolysis leading to MnO_2.

$$Mn^{2+}_{bulk} \longrightarrow Mn^{2+}_{ads} \qquad (rds)$$
$$Mn^{2+}_{ads} \longrightarrow Mn^{4+} + 2e^- \qquad (fast)$$
$$Mn^{4+} + 4H_2O \longrightarrow Mn(OH)_4 + 4H^+$$
$$Mn(OH)_4 \longrightarrow MnO_2 + 2H_2O \qquad (slow)$$

Further, Clarke *et al* [59] proposed two different mechanism for Mn(II) oxidation and revealed that with diluted acid concentration (<1M), very less Mn(III) is formed which undergoes hydrolysis to form MnOOH subsequently leading to MnO_2 precipitation. However, with concentrated acid electrolytes (>1M), the generated Mn(III) goes into the bulk leading to Mn(III)-Mn(III) collisions thereby giving rise to MnO_2.

2.4.1 Mn based RFBs:

There has been very few reports in the literature regarding the use of Mn electrolyte in RFBs. Lee *et al* [60] studied a V-Mn RFB displaying a higher energy density (31 Wh L^{-1}) as compared to V/V (21.1 Wh L^{-1}), owing to the high redox potential of Mn. However, the formation of MnO_2(s) during the charging resulted in the decrement of the energy density after 20 cycles. Further, Xue *et al* [37] investigated the electrochemical behavior of Mn(II)/Mn(III) redox couple on carbon felt and spectral pure graphite electrodes and mentions that disproportionation reaction of Mn(III) was evident on the carbon felt while it was quite weak on the latter due to its less active sites. They further observe a very high reversibility of Mn(II)/Mn(III) with increase in concentration of sulfuric acid (5M). The average discharge voltage was 14% higher and comparable energy efficiency (62.7%) was achieved with V/Mn system as compared to VRFBs. Further, Dong *et al* [61] reported a novel Ti-Mn RFB wherein they realized that upon mixing TiO^{2+} ions with Mn(II) in H_2SO_4 solution, they prevent the disproportionation of Mn(III) thereby reducing the particles size of MnO_2. They reported an energy density of 23.5 kWh m^{-3} with the Ti-Mn system that is comparable to the all VRFBs.

Chapter 3. Electrochemical methods

3.1 Cyclic Voltammetry:

Voltammetry is widely considered as an electroanalytical technique, providing information about the thermodynamics, kinetics and mechanism of an electrochemical reaction. It is generally performed in three-electrode configuration, consisting of working electrode (WE), counter electrode (CE) and reference electrode (RE) (Figure 3.1). The potential at working electrode is monitored vs. a reference electrode whereas the CE is used to balance the current flow at the WE. It is varied linearly with respect to time at a desired scan rate (in V/s) at positive and negative potential, taking the name cyclic voltammogram. The resulting current (i) at the working electrode is plotted *vs.* the potential applied (*E*) curve illustrating a cyclic voltammogram[62].
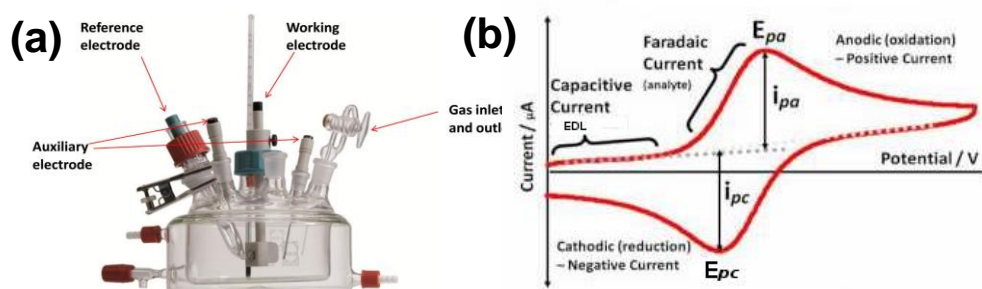

Figure 3.1: Schematic representation of (a) three electrode setup [62] (b) Resulting *I-E* curves, (cyclic voltammogram) for a reversible system [63]

Following the Randles-Sevcik relation (Equation 1), the maximum peak current is related to the square root of scan rate and the diffusion coefficient (*D*) of a particular analyte can be estimated. Moreover, the 1/2 slope of log (scan rate) vs. log (peak current) also indicates the process is diffusion controlled [58]. However, this relation is valid only for reversible redox couples.

$$Ip = (2.69 * 10^5)n^{\frac{3}{2}} A \, D^{\frac{1}{2}} \, v^{\frac{1}{2}} \, C^* \qquad (1)$$

where, *I*p = peak current (A), *n* = number of electrons, *A* = electrode area (cm^2), *D* = diffusion coefficient (cm^2/s), *C**= concentration (mol/cm^3) and *v* = scan rate (V/s).

3.2 Rotating Disk electrode (RDE):

In 1952, Benjamin Levich [64] first gave the models describing the theory for mass transport with the use of a rotating disk setup, which was experimentally confirmed by

Siver and Kabanov. They rigorously studied and solved the hydrodynamic and convective-diffusion equations for the rotating disk, in order to probe electrochemical reaction kinetics [64-65]. The RDE takes the advantage of a laminar flow from the bulk of the solution, conveying the analytes to the electrode surface, inducing the formation of diffusion layer. The diffusion layer is very thin with an approximate thickness given by the following relation *i.e.*

$$\delta\,(f) = \mathbf{1.61}\,D^{\frac{1}{3}}\,v^{\frac{1}{6}}\,\omega^{-1/2} \qquad\qquad (2)$$

Due to the continuous convection from the bulk of the solution, the rotating disk tends to induce a limiting current plateau, instead of decaying at zero, which is in the case of unstirred solutions. Increasing the rotation rate increases the rate at which analyte arrives at the electrode surface, thereby increasing the limiting current.

The limiting current observed with rotating disk is given by Levich equation *i.e.*

$$i_l = (\mathbf{0.62})\,n\,F\,A\,D^{\frac{2}{3}}\,\omega^{\frac{1}{2}}\,v^{-\frac{1}{6}}\,C^{*} \qquad\qquad (3)$$

where i_L = limiting current (A), n = number of electrons, ω = angular frequency (rad s^{-1}), v = kinematic viscosity (cm^2/s), F = Faraday constant (C/mol), D = Diffusion coefficient (cm^2/s), C^{*} = Analyte concentration (mol/cm^3).
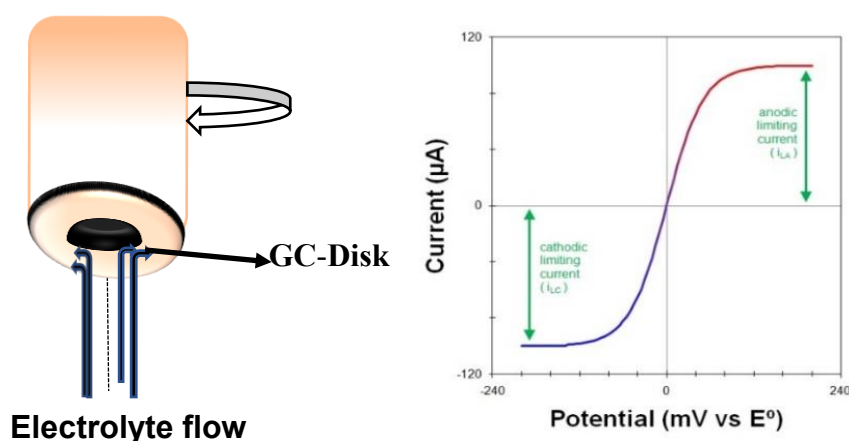

Figure 3.2 (a) Scheme of a rotating disk electrode (b) RDE voltammogram for both anodic and cathodic redox couples [64]

If an electrochemical reaction is reversible with no chemical process, the resulting voltammogram will be sigmoidal in shape irrespective of the rotation rate and the limiting current will be a linear function of square root of scan rate passing through the origin. For a redox reaction with sluggish kinetics, the kinetic parameters such as the

rate constant, transfer coefficient etc. can be estimated using the Koutecky-Levich relation [64] (Equation 4, 5) *i.e.*

$$\frac{1}{j} = \frac{1}{j_k} + \frac{1}{j_l} \qquad (4)$$

$$\frac{1}{j} = \frac{1}{j_k} + \frac{1}{0.620nFD^{2/3}\omega^{1/2}\,\nu^{-1/6}C} \qquad (5)$$

where, j is the total current density, j_k is kinetic current density and j_l is the limiting current density, whereas all other parameters has their usual significance as mentioned above.

The reciprocal of limiting current density is plotted against reciprocal of rotation rates and the kinetic current density can be obtained from the intercept of the plot. The overpotential relates to the kinetic current density according to the (Equation 6). The plot of over potential *vs* log kinetic current density is equal to the log of exchange current density from which k^o was estimated (Equation 7).

$$j_k = Fk_f(E)C^* \qquad (6)$$

where k_f = heterogeneous rate constant (cm s^{-1}), C^* = bulk concentration (moles cm^{-3}), E = potential, j_k = kinetic current density.

$$k_f = k^o exp[-\alpha f(E - E^o] \qquad (7)$$

where k^o = standard rate constant (cm s^{-1}), α = transfer coefficient, $E - E^o$ = overpotential, f = Faraday constant

3.3 <u>Rotating ring disk electrode (RRDE)</u>:

Alexander Frumkin with his colleague, Lev Nekrasov developed the idea of installing a concentric ring around the rotating disk in 1958. The idea of placing ring adjacent to the disk was thought in order to detect the products generated from the half-cell reaction at the disk electrode. RRDE provides information about two key parameters including the collection efficiency (*N*) and transit time. The ring to disk current ratio for a particular reaction determine its "collection efficiency" which is used to elucidate the amount of product generated at the disk electrode with its subsequent detection on the ring (Equation 9). In general, the ring-disk geometry typically has a collection

efficiency of 20-30% [64]. However, transit time indicates the average time travelled by the species after reacting at the disk electrode and being detected at the ring, and is a function of both the rotation rate and the distance between the disk and ring electrodes [64, 66].
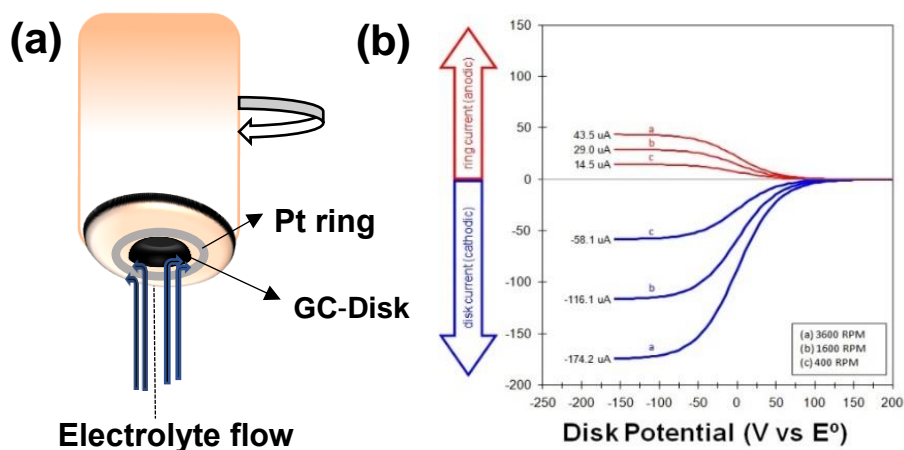
$$N = \frac{-i_{Ring}}{i_{Disk}} \qquad\qquad (8)$$

(a)

Pt ring

GC-Disk

Electrolyte flow

(b)

Figure 3.3 (a) Scheme of a rotating ring disk electrode (b) RRDE voltammogram at different rotation rates [64]

Chapter 4. Experimental Section

4.1 <u>Chemicals and solutions:</u>

Manganese sulfate monohydrate ($MnSO_4 \cdot H_2O$), Titanium oxysulphate solution ($TiOSO_4$, ~15 wt. % in dilute sulfuric acid), Vanadium Pentoxide (V_2O_5) and Sulfuric acid (ISO 95-97 %) were purchased from Sigma Aldrich, Switzerland. The acid solutions were prepared by diluting concentrated sulfuric acid (95 – 97%) into ultrapure water. The mixed electrolyte solutions of V-Mn-Ti is in turn prepared via dissolving equimolar ratio of pale pink ($MnSO_4 \cdot H_2O$) and orange (V_2O_5) salt in 5M sulfuric acid at room temperature. The VO_2^+ solution is sonicated and stirred for approximately 2-3 hours in order to solubilize in water-sulfuric acid mixture. The concentration of electrolytes used is mentioned in table 1.4.

Electrolyte	$MnSO_4.H_2O$ (M)	$TiOSO_4$ (M)	VO_2^+ (M)	H_2SO_4 (M)
$MnSO_4. H_2O$	0.1	0	0	5
$TiOSO_4$	0	0.1	0	5
VO_2^+	0	0	0.1	5
$VO_2^+ + MnSO_4$	0.1	0	0.1	5
$TiOSO_4 + MnSO_4$	0.1	0.1	0	5
$TiOSO_4 + MnSO_4 + VO_2^+$	0.1	0.1	0.1	5

Table 4: Concentration of Electrolytes

4.2 <u>Electrochemical Protocol:</u>

Electrochemical analysis were done using cyclic voltammetry (CV), rotating disk electrode (RDE), rotating ring disk electrode (RRDE). All measurements were performed at ambient temperature with an Autolab PGSTAT potentiostat-galvanostat (Metrohm, Switzerland). CV were performed with a three electrode setup using glassy carbon (0.071 cm^2) as working electrode, platinum mesh as a counter electrode with reference electrode as Ag/AgCl (3M KCl). Rotating electrodes were supplied from Metrohm and included GC disk electrode (RDE), and GC Disk-Pt ring (RRDE) as working electrode. The diameter of the disk was 5mm (r_1), with the inner and outer diameter of the ring to be 5.75 (r_2) and 6.5mm (r_3) respectively. The geometrical area of the disk and ring electrodes were 0.196 cm^2 and 0.07 cm^2 respectively. Before using, the electrodes were polished using alumina paste (1 μM) and thoroughly rinsed with Milli-Q water followed by drying with a lint free tissue. For the RDE experiment,

the disk electrode was swept from 0 to 2 V and 2.5V at 10 m Vs^{-1}. When an RRDE experiment was conducted the Pt ring was set at 0.6V and 1V. Carbon felt electrodes (4cm^2) were also used for surface characterization, which were pre-treated by heating in an oven at 400°C for 4 hours. To image the plating of MnO_2(s), chronoamperometry was performed by applying a potential of 1.6 V for 30 minutes on flat glassy carbon electrodes with an area of 1cm^2 in a 10mM solution of the different electrolyte in 50 mM H_2SO_4 to ensure the plating. Scanning electron microscope (SEM) from FEI model Teneo was utilized with a Schottky field emission gun. The SEM is equipped with an Everhart-Thornley detector (ETD) for secondary electrons, two in column detectors for backscattered electrons and an energy-dispersive X-ray spectroscopy detector from Bruker. The H-cell setup was used to perform first electrochemical oxygen evolution reaction test on MnO_2 by applying a potential of 1.8 V vs. Ag/AgCl (KCl 3M). It was operated like a three electrode setup with the reference electrode placed on the positive side. The volume of positive analyte employed was 5mL. The positive and negative tanks were separated by glass wool. Further, the charged Mn(III) electrolyte was mixed with IrO_2 catalyst whilst stirring to observe the increase in voltage signal attributing to oxygen evolution.

Chapter 5. Results and Discussion

4.1 <u>Cyclic Voltammetry Studies:</u>

4.1.1 Mn(II)/Mn(III) redox reaction:

To study the Mn(II)/Mn(III) redox reaction, cyclic voltammetry with 0.1 $MnSO_4.H_2O$ in 5M H_2SO_4 were performed on GC electrode. An oxidation peak at 1.64 V and one reduction peak at 1.08 V *vs.* SHE were observed (Figure 4.1a). The oxidation peak at about 1.64 V is attributed to the oxidation of Mn(II) to Mn(III). After the oxidation, a spontaneous disproportionation of Mn(III) occurs. During the reverse scan, Mn exists in three redox states Mn(II), Mn(III) and $MnO_{2(S)}$. As reported[37] the reduction peaks at 1.08 V is attributed to $MnO_2(s)$/Mn(II) reaction. However, it was noticed that with increase in scan rate to 1 V s^{-1}, a small reduction peak appears at 1.49 V *vs.* SHE (see appendix 1.1). The peak can be due to Mn(III) to Mn(II) reduction, indicating that the disproportionation reaction is a rate limiting process. This was further confirmed by the decrease in charge ratio for both the peaks with increase in scan rate. It was understood that the Mn(II)/Mn(III) reaction proceeds through an ECE mechanism *i.e.* a reversible electrochemical oxidation of Mn(II) to Mn(III) followed by an irreversible chemical reaction of Mn(III) intermediates with the solvent to form $MnO_2(s)$ and Mn(II) [58-59]. The slope of log (peak current) vs. log (scan rate) was calculated to be 0.34, suggesting that the process is diffusion controlled. (Figure 4.1b)
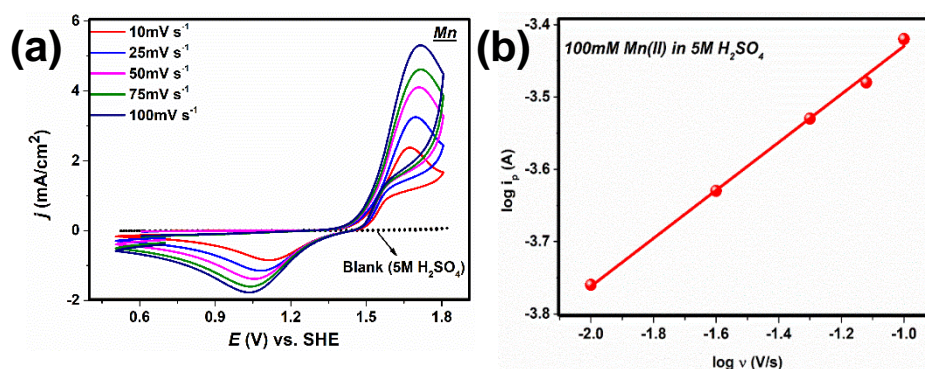

Figure 4.1 (a) cyclic voltammogram of 100mM $MnSO_4.H_2O$ in 5M H_2SO_4 at different scan rates. (b) Plot of log (peak current) vs. log (scan rate). Conditions: glassy carbon electrode.

4.1.2 Study of the influence of $TiOSO_4$ on Mn(II)/Mn(III) reaction:

It was previously reported [61] that Mn(III) can be stabilized upon mixing TiO^{2+} ions with Mn(II) in concentrated H_2SO_4 solution preventing the disproportionation reaction.

Therefore, in order to understand the redox mechanism behind the inhibition of MnO_2 formation by addition of TiO^{2+} in the electrolyte, concentration dependence study of $TiOSO_4$ was done keeping the concentration of $MnSO_4$ to be 0.1M in 5M H_2SO_4 (Figure 4.2a). An oxidation peak was observed at potential of about 1.61 V and one reduction peak at 0.9-1.08 V *vs.* SHE when scanning in the reverse direction at 10 mV s^{-1}. Similar behaviour with appearance of a small reduction peak at 1.5 V *vs.* SHE while scanning at 1 V s^{-1} was observed (see appendix 1.1). With an increase in concentrations of $TiOSO_4$, the faradaic current of oxidation and reduction increases but after a certain ratio i.e. 200mM to 500mM, the current starts to decrease which might be due to the complexation of both redox species [43].
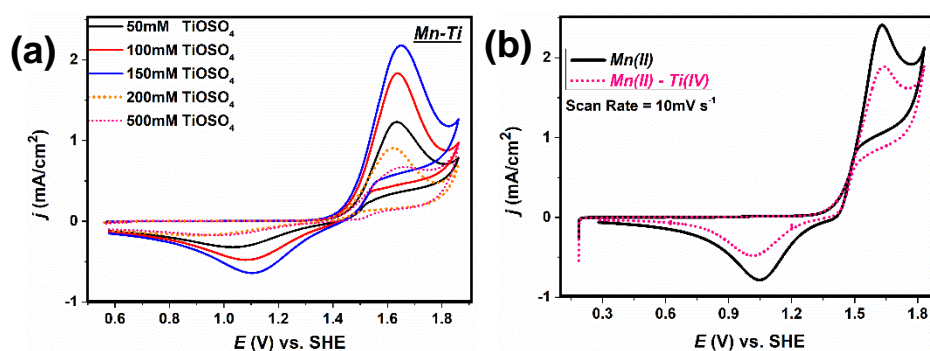

Figure 4.2. Cyclic Voltammogram of (a) 0.1M Mn and (b) 0.1M Mn-Ti in 5M H_2SO_4. Conditions: scan rate: 10mV/s. working electrode: glassy carbon.

Ranging the concentration of Ti(IV) didn't gave an insight about the Mn(III) stabilization, therefore, further studies were done with a particular ratio of 1:1 (Mn:Ti). From the CV studies with Mn(II)-Ti(IV) electrolyte (Figure 4.2b), it can be hypothesized that adding TiO^{2+} ions indeed reduce the particle size of MnO_2 resulting in less plating on the electrode as compared to the Mn(II) electrolyte [61].

4.1.3 Study of the mixed electrolyte of V-Mn and V-Mn-Ti:

Lee and co-workers[60] studied the effect of $MnO_2(s)$ precipitation with a V/Mn redox flow battery and reported that during the course of battery cycling, vanadium from the negative side permeates to the positive side thereby reducing the $MnO_2(s)$ to Mn(II) ions, acting as a positive active material. However, it was not studied in detail. Therefore, in order to study the influence of vanadium ions on the disproportionation reaction of Mn(III), cyclic voltammetry at different scan rate were done with 0.1M V(V), 0.1M V(V)-Mn(II) followed by a mixed electrolyte of 0.1M V(V)-Mn(II)-Ti(IV) (see appendix 1.2). The oxidation of V(IV) to V(V) occurs at 1.2 V while its reduction

occurred at 0.9 V *vs.* SHE. The slope obtained for log (peak current) vs. log (scan rate) was 0.5, indicative of a diffusion-controlled process (see appendix 1.2). Mn(II) was added in the vanadium electrolyte and CVs were performed. The V(IV) to V(V) oxidation at 1.2 V *vs.* SHE was followed by the Mn(II) to Mn(III) oxidation at 1.65 V (Figure 4.3). The peak current density for Mn(II) oxidation was low to be 1.45 mA cm^{-2} as compared to Mn(II) and Mn(II)-Ti(IV) electrolyte. With the addition of Ti(IV) in V-Mn electrolyte, there was a slight increase in the peak current density for the oxidation of vanadium and manganese as compared to the V-Mn electrolyte. The disappearance of the reduction peak from MnO_2(s) to Mn(II) at 1.1 V can be due to the overlap of vanadium (V) reduction at similar potentials for the latter cases. The CV studies did not provide much understanding regarding the stabilization of Mn(III), however the extent of MnO_2 plating seems to be reduced with the incorporation of Ti(IV) and V(V), attributed to the decrease in current. It will be further studied by rotating disk electrode (RDE) and rotating ring disk electrode (RRDE).
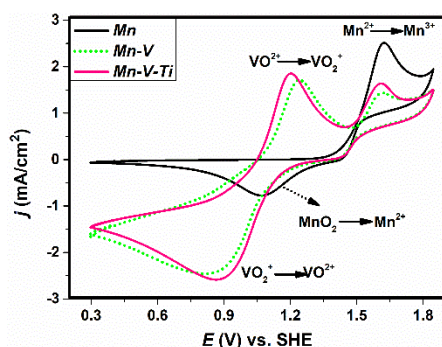

Figure 4.3. Cyclic Voltammograms of 0.1M V(V), Mn(II) and Ti(IV) with 5M H$_2$SO$_4$. Conditions: scan rate: 10mV/s, working electrode = glassy carbon.

4.2 <u>Rotating disk electrode (RDE) studies</u>:

4.2.1 Mn(II)/Mn(III) redox reaction:

Rotating-disk electrode (RDE) studies were performed in order to not get limited by diffusion of reduced species from the bulk of the solution and to study whether it was possible to stabilize Mn(III) by adding TiOSO$_4$ or VO$_2^+$ in Mn(II) electrolyte.

A single anodic peak and cathodic peak were observed at 1.68 V and 1.5 V *vs.* SHE respectively (Figure 4.4a). It can be inferred that the peak at 1.68 V resulted from the oxidation of Mn(II) to Mn(III) and to its disproportionation to form MnO_2(s). RDE experiments are expected ideally to show a sigmoidal S shape curve (limiting current

plateau) but it was not observed in this case due to the disproportionation of Mn(III). Increase in rotation speed forms a film of MnO_2 leading to passivation of the disk electrode. The sharp reduction peak at 1.5 V results in cathodic stripping of the oxide layer from the electrode surface. According to the Levich (Equation 3), a linear relation between i_L (limiting current) and ω (angular frequency) that passes through origin indicates that the system being studied is under mass transport control. Figure 4.4b illustrates the Levich plot obtained from the RDE voltammogram where the peak current value was used as limiting current. A large deviation from origin further confirmed the electrochemical-coupled chemical process during the oxidation of Mn(II). The diffusion coefficient of Mn(II) was calculated by plotting the peak current density as a function of square root of rotation rate. It exhibited straight line following the Levich equation yielding a $D_{Mn(II)} = 1.57 \cdot 10^{-7}$ cm^2 s^{-1}, indicating a reasonably fast diffusion of Mn(II) species. The value obtained was comparable to what is mentioned in the literature by Guidelli and Piccardi in 15N H_2SO_4, $D_{Mn(II)} = 0.9 \cdot 10^{-6}$ cm^2 s^{-1}. There
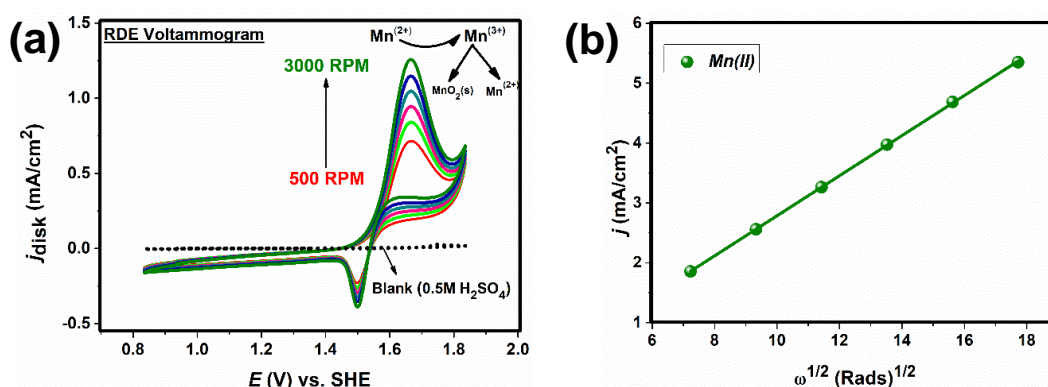
were no reports in literature regarding the diffusion coefficient of Mn(II) with 5M H_2SO_4.

Figure 4.4. (a) RDE voltammogram (CV) for 0.01M MnSO₄.H₂O in 0.5M H₂SO₄. (b) Levich plot obtained from (a).

The rate constant (k^o) and transfer coefficient (α) estimated from Koutecky-Levich analysis (Equation 6, 7) for Mn(II)/Mn(III) reaction were $2.73 \cdot 10^{-5}$ cm s^{-1} and 0.61 respectively further suggesting a reasonably fast redox reaction (Figure 4.5a, b). The diffusion coefficient and rate constant calculated for different electrolyte are mentioned in Table 1.5. It can be said that with Mn-Ti, Mn-V and Mn-V-Ti electrolytes, a diffusion coefficient of same order (10^{-8} cm^2 s^{-1}) along with the rate constant (10^{-5} cm s^{-1}) was achieved. However, it was observed that with the addition of Ti(IV), the value obtained was relatively low as compare to when V(V) was added with Mn(II), with V-Mn-Ti being

the lowest. Although, it was lower than what is achieved with only Mn(II) electrolyte only (10^{-7} cm^2 s^{-1}).
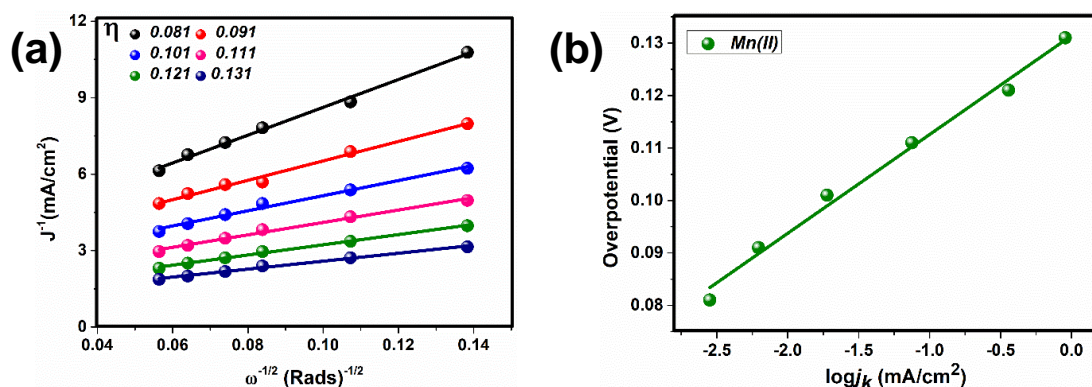

Figure 4.5. (a) Koutecky-Levich plot at different overpotentials (b) plot of overpotential vs log of kinetic current density.

Redox Species	Diffusion coefficient (cm^2/s)	Rate constant (cm/s)
Mn(II)	$1.57 \cdot 10^{-7}$	$2.73 \cdot 10^{-5}$
Mn(II) – Ti(IV)	$4.47 \cdot 10^{-8}$	$6.55 \cdot 10^{-5}$
V(V)	$3.21 \cdot 10^{-7}$	$1.80 \cdot 10^{-5}$
Mn(II) – V(V)	$3.74 \cdot 10^{-8}$	$4.53 \cdot 10^{-5}$
Mn(II) – V(V) – Ti(IV)	$7.12 \cdot 10^{-8}$	$8.59 \cdot 10^{-5}$

Table 5: Parameters extracted from RDE experiment for Mn(II) oxidation on GC electrode.

Clarke et al [59] reported that with dilute concentration of sulfuric acid (0.1M) the hydrolysis product of Mn (III) or MnO$_2$(s) deposits on the surface of the electrode very rapidly. To reduce the plating of MnO$_2$(s) on the electrode surface, the concentration of sulfuric acid was increased to 5M thereby depositing less manganese oxide on the electrode surface (Figure 4.6a). Rotation rate studies was performed and it was observed that peak current density decreased with increase in rotation rate. This suggests that after the first rotation rate, due to the disproportionation of Mn(III), the disk gets covered with traces of MnO$_2$(s), spoiling the clean GC surface, restraining the current flow. The crossover during the reverse scan was thought to be either due to the stripping or due to the removal of MnO$_2$(s) traces from the electrode. However, this behavior was not observed for the linear sweep voltammetry (LSV). Figure 4.6b displays the LSV obtained for the Mn(II) oxidation on glassy carbon and platinum disk. The onset for oxidation plateau concerning Mn(II) was observed at 1.54 V *vs.* SHE. A steep increase in the peak was observed at 1.85 V for the GC and 1.79 V with the Pt electrode-giving rise to an S shape curve. However, it started quite early requiring less

overpotential with the platinum due to its high catalytic active surface. The maximum current density obtained for Mn(II) oxidation on glassy carbon and platinum disk was 14.8 mA cm^{-2} and 28.14 mA cm^{-2} respectively.
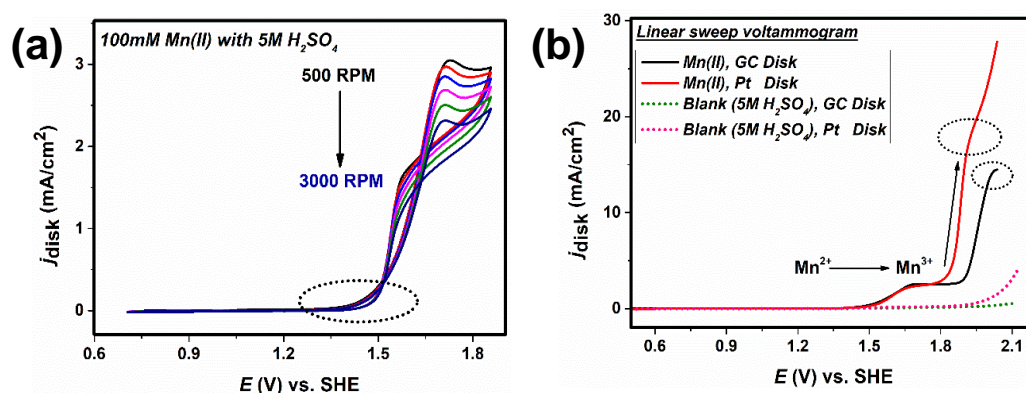

Figure 4.6. RDE voltammogram a) CV b) LSV for 0.1M MnSO$_4$.H$_2$O in 5M H$_2$SO$_4$. Conditions: GC and Pt disk electrode.

In order to confirm the origin of the current increase after 1.9 V *vs.* SHE, the potential window was increased to 2.5 V *vs.* SHE and LSVs were recorded (Figure 4.7). The scan started from 1.2 V and was swept in the anodic direction. With only Mn(II) in the system, the onset potential of its oxidation to Mn(III) was 1.54 V *vs.* SHE exhibiting a plateau, with an abrupt jump at 1.89 V reaching a maximum peak current density of 19.87 mA cm^{-2} at 2.08 V. This was followed by a decrease in the current at 2.1 V forming a peak. Appearance of peak at a very high potential of 2.08 V can be accredited to the platting of MnO$_2$ on the disk electrodes, resulting in the abrupt jump reaching a high current density. Alternatively, it can be due to the oxidation of Mn(II) to Mn(IV) due to the continuous convection from the bulk of the solution. However, it was not confirmed. Ranging the potential window above 2.28 V *vs.* SHE resulted in a steep increase of the peak, reaching a maximum current density of 115 mA cm^{-2}, accounting for the oxygen evolution reaction (OER).

4.2.2 Study of the influence of TiOSO$_4$ on Mn(II)/Mn(III) reaction:

Further, RDE was performed with Ti(IV)-Mn(II) electrolyte (Figure 4.7). The onset potential for Mn(II) to Mn(III) oxidation was 1.54 V *vs.* SHE, reaching a limiting current plateau at 1.7 V. Similar behavior was observed with an appearance of a peak at 2.04 V with respect to only Mn(II) electrolyte. However, it should be noted that the current density achieved was lower for both the plateau as well as the peak to be 2.41 mA cm^{-2} and 14.53 mA cm^{-2} respectively at 2.01 V. It can be said that the decrease in peak

current density is accounted for the reduction in plating of MnO_2 particles with the addition of TiO^{2+} ions. Similar behavior in the appearance of the peak at 2.28 V, corresponding to OER was observed. The diffusion coefficient and rate constant obtained for the Mn-Ti electrolyte was calculated to be $4.47 \cdot 10^{-8}$ cm^2 s^{-1} and $6.55 \cdot 10^{-5}$ cm s^{-1} respectively. The values obtained were quite low as compared to the only Mn(II) electrolyte suggesting a relatively slow diffusion of Mn(II) species with the addition of Ti(IV), with the overall reaction preceding at a slow rate.

4.2.3 Study of the mixed electrolyte of V-Mn and V-Mn-Ti:

With the addition of V(V) in the Mn(II) electrolyte, the reaction proceeds via reduction of V(V) to V(IV) at 1 V vs. SHE, followed by Mn(II) to Mn(III) oxidation at 1.54 V vs. SHE reaching similar currents with Mn-Ti electrolyte for the limiting current plateau (Figure 4.7). However, it was observed that, instead of a peak at 2.04 V, observed with only Mn(II) and Mn(II)-Ti(IV), a steady state plateau was observed in the case of V-Mn electrolyte. The current density for the same was 6.84 mA cm^{-2}, which is almost 3 times lower than what was achieved with only Mn(II) electrolyte. The diffusion coefficient (D) and rate constant (k^o) for the V(V)-Mn(II) electrolyte was calculated to be $3.74 \cdot 10^{-8}$ cm^2 s^{-1} and $4.55 \cdot 10^{-5}$ cm s^{-1} respectively which is higher than in the case of Mn-Ti electrolyte indicating that diffusion of Mn(II) occurs relatively more fast with V(V) as compared to Ti(IV).

In the case of V-Mn-Ti electrolyte, a decrease in the current density for the V(V) to V(IV) reduction as well as for the Mn(II) to Mn(III) oxidation was observed (Figure 4.7). A linearly decreasing plateau at 2.07 V was observed with mixed electrolyte of V-Mn-Ti, exhibiting a shift of 40mV for the onset. The peak current densities further decreased to 1.53 mA cm^{-2} for the Mn(II) oxidation while 4.57 mA cm^{-2} for the peak at 2.07 V respectively. Further, the V-Mn-Ti electrolyte displayed the lowest diffusion coefficient (D) and rate constant (k^o) to be $7.12 \cdot 10^{-8}$ cm^2 s^{-1} and $8.59 \cdot 10^{-5}$ cm s^{-1} respectively as compared to the other four electrolytes (Mn, Mn-Ti, Mn-V and V) studied. This indicates that with the addition of Ti(IV) in the electrolyte, the reaction kinetics is slowed down for the Mn(II) to Mn(III) oxidation, with a lower diffusion rate of Mn(II) species.
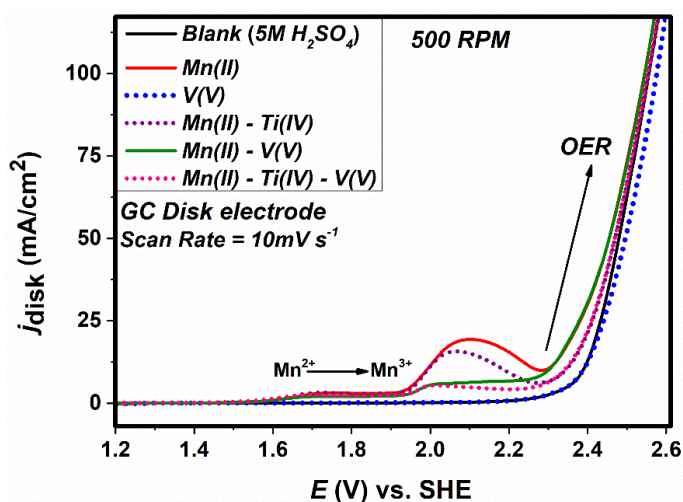
Figure 4.7. RDE voltammogram (LSV) for 0.1M Mn, Mn-Ti, Mn-V, Mn-Ti-V in 5M H$_2$SO$_4$.

The present RDE studies indicates that due to the continuous convection from the bulk of the solution at the electrode, there can be two possible oxidation process occurring i.e. Mn(II) to Mn(III) at 1.54 V whereas Mn(II) to Mn(IV), at 2.1 V *vs.* SHE. This is followed by an oxygen evolution reaction at 2.3 V with all the five electrolytes studied, along with the blank (5M H$_2$SO$_4$), suggesting that the peak at 2.28 V is not a catalytic peak but the oxidation of the electrolyte itself on glassy carbon at very high potentials. The disproportionation reaction of Mn(III) is so fast that it cannot be restrained with the addition of Ti(IV) or VO$_2^+$. However, the extent of MnO$_2$ plating was reduced with the addition of these two ions, with the former having more effect due to large decrease in current density for both the peaks resulting in a limiting current plateau for the oxidation of Mn(II) to Mn(IV).

As we made a hypothesis regarding the plating of MnO$_2$ in this section, surface characterization of MnO$_2$ on the electrode surface with the help of SEM was performed to study weather adding Ti(IV) really helps in reducing the disproportionation as reported in the literature or does V(V) is better in stabilizing Mn(III).

4.3 Rotating-ring disk electrode (RRDE) studies:

RRDE takes the advantage of a second working electrode *i.e.* a ring placed along the central disk, used to detect products and intermediates generated at the disk, providing information about multi-electron transfer process and mechanisms for various electrochemical reactions. In order to extract collection efficiency for the Mn(II)/Mn(III) redox reaction, RRDE was performed. In this experiment, a 4-electrode

setup [WE(1): Disk, WE(2): Ring, CE: Pt wire, RE: Ag/AgCl (KCl 3M)] was used to simultaneously measure the oxidation and reduction of Mn(II) with different ratios of Ti(IV) and V(V) at different scan and rotation rates. The maximum theoretical collection efficiency for this system was 25%. It was estimated using the RRDE geometry *i.e.* the outer diameter of the disk along with the inner and outer diameter of the ring, and is independent of the rotation rate. Detailed calculation for the theoretical collection efficiency is mentioned in Appendix.

4.3.1 Mn(II)/Mn(III) redox reaction:

Figure 4.8(a) shows RRDE (CV) with 0.1M Mn(II) in 5M H_2SO_4. Here, the ring was kept at a constant potential of 0.6 V while the disk was swept in the anodic direction from 0.7 V to 1.9 V *vs.* SHE. The maximum disk and ring current density achieved were 3 mA cm^{-2} & -1.75 mA cm^{-2} respectively. Symmetrical shape was observed with respect to the ring and disk currents. The crossover during the reverse scan was thought to be either due to the stripping or due to the removal of MnO_2(s) traces from the electrode. However, the sharp stripping peak was not observed with an increase in the concentration of sulfuric acid to 5M (dotted circle). Collection efficiency (*N*) of 22.61 % was achieved with Mn(II) electrolyte at 0.6 V. The reason for the above was thought to be the reduction of MnO_2(s) to Mn(II), (as mentioned in voltammetry studies), explaining a collection efficiency close to the theoretical value. As we were interested to gain information about Mn(III) to Mn(II) reduction, the ring potential was varied to gain information about the potential ranges where it was maximum. To eliminate the risk of reducing MnO_2(s) to Mn(II), the ring potential was fixed to 1V for further measurements.
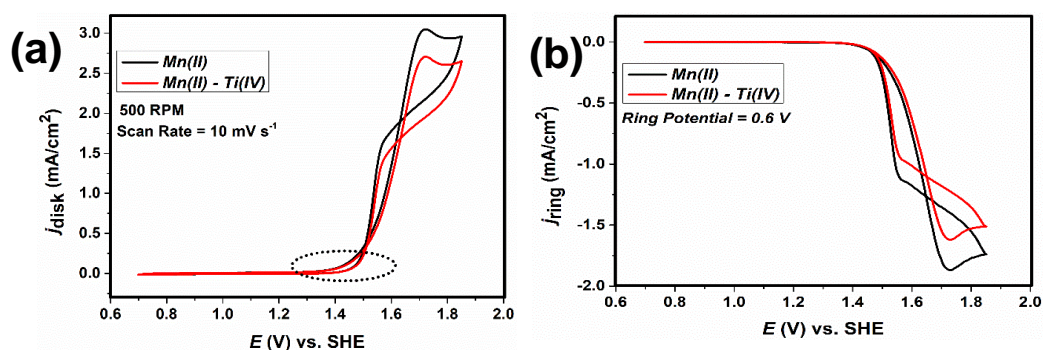

Figure 4.8. RRDE voltammogram (CV) for 0.1M MnSO₄.H₂O and 0.1M TiOSO₄ in 5M H₂SO₄ a) disk current b) ring current. Condition: glassy carbon disk, platinum ring.

An approximate steady state plateau was observed with the first rotation rate during the LSV measurements performed with Mn(II) electrolyte (see appendix 1.4). With an increase in the rotation rate (1247 RPM), appearance of a peak was observed which was accounted to the passivation of disk electrode due to the disproportionation of Mn(III). The maximum current density at 500 RPM for the disk and ring achieved were 2.24 mA cm^{-2} and -0.12 mA cm^{-2} respectively. The collection efficiency decreased with increase in rotation speed and an average collection efficiency obtained for Mn(II) electrolyte was quite low to be 2.91 % owing to the large extent of disproportionation.

4.3.2 Study of the influence of TiOSO$_4$ on Mn(II)/Mn(III) reaction:

The RRDE for the Mn(II)-Ti(IV) electrolyte displayed similar behavior, with respect to decrease in peak current density for both disk and ring as the rotation speed was increased (Figure 4.8a). Collection efficiency of 21.9 % was achieved with Mn-Ti electrolyte when the ring potential was 0.6 V. With LSV the currents increased with increase in rotation speed, contrary to what was observed with CVs (see appendix 1.4). The disk and the ring current densities were low to be 1.81 mA cm^{-2} and -0.07 mA cm^{-2}, as compared to Mn(II) electrolyte. Symmetrical response with respect to the shape of ring currents were observed with disk currents with an order of almost ten time's lower magnitude for the former due to the low area of the ring electrode. An average collection efficiency of 1.32 % was achieved with the Mn-Ti electrolyte, at ring potential of 1 V, lower than when only Mn(II) was present (Figure 4.9). It was hypothesized that after the oxidation of Mn(II) to Mn(III), the generated Mn(III) complexes with the TiO^{2+} ions while a certain ratio of Mn(III) undergoes disproportionation to form a film of MnO$_2$(s) on the surface of electrode altering its surface.

4.3.3 Study of the mixed electrolyte of V-Mn and V-Mn-Ti:

Further, V(V) was mixed with the Mn(II) electrolyte and RRDE was performed keeping the ring potential fixed at 1 V (Figure 4.9). The disk currents were quite similar to what was observed with the RDE. At the start of the scan, the negative disk current represents the V(V) to V(IV) reduction followed by the oxidation of Mn(II) to Mn(III) at 1.54 V $vs.$ SHE. However, the currents obtained on the ring were also negative, achieving a maximum current density of -0.2 mA cm^{-2} for the Mn(III) to Mn(II) plateau at 1.67 V, followed by a dip in current at 1.84 V. The average collection efficiency

obtained with V-Mn electrolyte was 1.81 %, almost what was achieved with Mn-Ti, but still lower than the Mn(II) electrolyte. Further, when Ti(IV) was added in the V-Mn electrolyte, the disk current for the V(V) to V(IV) reduction as well as for the Mn(II) to Mn(III) oxidation were low to be -11 mA cm^{-2} and 1.12 mA cm^{-2} as compared to V-Mn electrolyte (Figure 4.9). The ring current density observed for the Mn(III) to Mn(II) reduction at 1.67 V was -0.34 mA cm^{-2}, which was the highest as compared to other three electrolytes at a ring potential of 1 V. An average collection efficiency of 4.81 % was achieved. The RRDE studies did not proved to be beneficial, as the collection efficiency achieved with all the four electrolytes were quite low, therefore it was difficult to comment about the optimum electrolyte which was significant for Mn(III) to Mn(II) reduction.
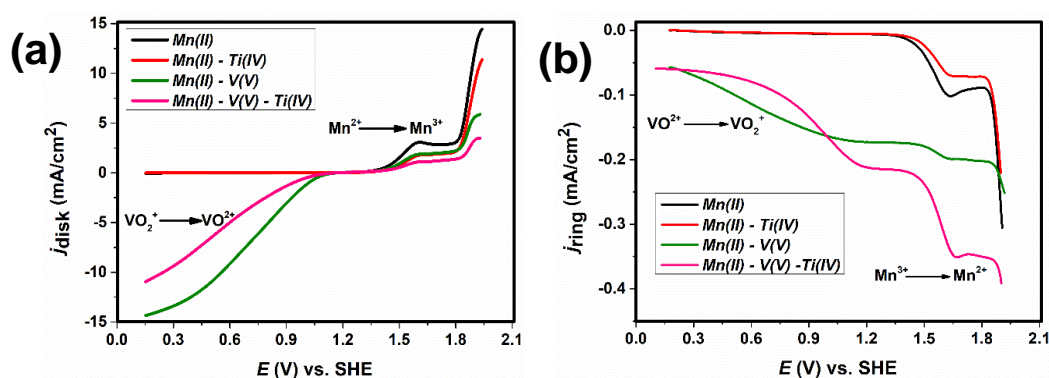

Figure 4.9 RRDE study for the 100 mM concentration equimolar ratio of the different electrolytes in 5M H$_2$SO$_4$ obtained at the a) disk b) and at the ring. Conditions: glassy carbon disk, platinum ring.

4.4 <u>SEM characterization</u>:

To image the plating of MnO$_2$(s) due to the disproportionation of Mn(III), chronoamperometry was performed by applying a potential of 1.6 V for 30 minutes on glassy carbon electrode in a 10mM solution of the different electrolyte (equimolar ratio) in 50 mM H$_2$SO$_4$ (Figure 4.10). A maximum current density of 0.094 mA cm^{-2} was achieved with Mn(II) electrolyte, followed by a decrease in current density with the addition of Ti(IV) to be 0.081 mA cm^{-2}. With V-Mn and V-Mn-Ti electrolyte, the current densities were almost similar to be 0.069-0.051 mA cm^{-2}, two times lower than what was observed with Mn(II) electrolyte after 30 minutes. The current densities were in the similar order, of what was observed with the rotating disk studies for different electrolytes.
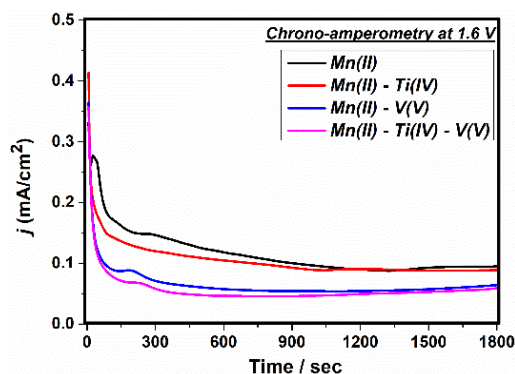
Figure 4.10 Chronoamperometry at 1.6 V for 30 minutes with 0.1 Mn(II), 0.1M Mn(II)-Ti(IV), 0.1M Mn(II)-V(V), 0.1M Mn(II)-Ti(IV)-V(V). Conditions: scan rate: 10mV/s, working electrode: glassy carbon.

Figure 4.11a, shows the SEM picture for the Mn(II) electrolyte on glassy carbon electrode. A thick film of MnO_2 was observed on the electrode surface with the presence of cracks all over it. A spherical shape, small bulbous like particle was observed with a diameter of about 1 μM. The presence of cracks was thought to be due to the evaporation of the solvent from the electrode surface during the preparation of the electrode. However, the plating was more significant on the carbon felt as the product of disproportionation can diffuse more rapidly into the porous holes, figure 4.12a.

When Ti(IV) was added in the electrolyte, plating of MnO_2 was still observed but it was reduced to quite an extent. An interaction of TiO^{2+} ions with Mn(III) and Mn oxides is also possible, resulting in the decrease in the particle size of MnO_2(s), as reported in the literature [61]. Again, the reduction in plating was significantly observed on the carbon felt, with traces of MnO_2 still visible on the carbon fibers, figure 4.12b.

In the case of V-Mn electrolyte, the morphology of the plated MnO_2 was quite different as compared to Mn and Mn-Ti electrolyte (Figure 4.11c). The presence of small particles with size below 1 μM was observed overall on the glassy carbon surface. Aggregation of particles to form clusters of oxides was observed. It can also be due to the formation of complex in between Mn and V species. However, it was not confirmed. The presence of small cracks observed on the MnO_2 film without Ti(IV) also supported the above statement.

With V-Mn-Ti electrolyte, the nucleation growth was quite different as compared to the Mn electrolyte since bigger nuclei were observed (Figure 4.11d). A slight change in

the morphology of the aggregates formed were noticed as compared to V-Mn electrolyte. Spots of MnO_2 stuck on the carbon fibers were imaged on carbon felt with V-Mn-Ti, however the overall plating of MnO_2 was lower as compared to other three electrolytes (Figure 4.12d).
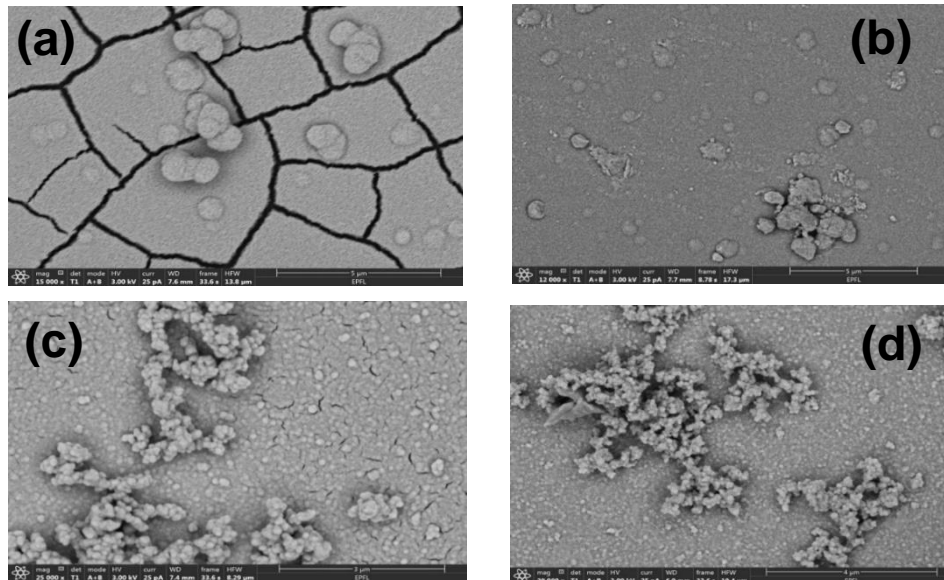

Figure 4.11. SEM pictures of a) Mn(II) b) Mn-Ti c) Mn-V d) Mn-V-Ti electrolytes on glassy carbon electrode.
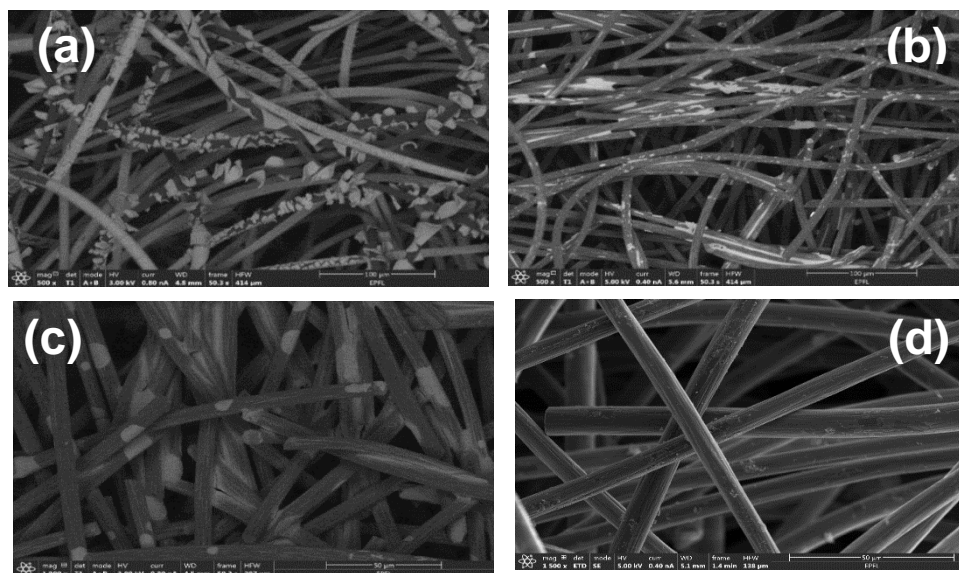

Figure 4.12. SEM pictures of a) Mn b) Mn-Ti c) Mn-V d) Mn-V-Ti electrolytes on carbon felt electrode.

From the present SEM studies, it can be said that a substantial plating of oxides were observed with Mn(II) electrolyte. With the addition of Ti(IV) the thickness of the oxide layer was reduced and less plating of MnO_2 was observed, suggesting that the presence of TiO^{2+} ions indeed reduced the particle growth of $MnO_2(s)$. The plating

39

observed was even less on addition of vanadium, however an aggregate of particles was observed on glassy carbon electrode which can be due to the formation of V-Mn complex. However, it was not confirmed. The mixed electrolyte of V-Mn-Ti displays the lowest MnO_2 deposition, with a distinct morphology of aggregate formation on glassy carbon substrate.

4.5 H-cell Test:

In order to test the feasibility of Mn(II) electrolyte for the oxygen evolution, a H-Cell test was performed with 5 mL of positive analyte (*i.e.* 0.1M $MnSO_4$ in 5M H_2SO_4) using carbon felt electrodes. The H-cell was operated like a three electrode setup whilst the reference electrode was placed to monitor the reaction at the positive side (Figure 4.13a). A calibration curve was done while injecting different volume of air through syringe in the range 0-1.8mL, while observing the increase in voltage signal (see appendix 1.5). The calibration curve was used to convert the voltage signal displayed by the pressure sensor to volume of oxygen produced. The Mn(II) electrolyte was charged (50 C) at 1.8 V *vs.* Ag/AgCl (KCl 3M) in order to generate Mn(III). Further, 50mg of IrO_2 catalyst was added in the charged Mn(III) electrolyte and was kept on stirring. The reaction proceeded quite fast, observed with the change in the color of the electrolyte to dark pink, attributing to presence of Mn(III). The OER efficiency was monitored with the increase in the pressure of the positive side, eventually reaching a plateau. Approximate volume of oxygen produced was around (1-1.1 mL) (Figure 4.13b). It can be said that Mn(II)/Mn(III) couple indeed facilitate oxygen evolution, albeit low efficiency, owing to the disproportionation reaction of Mn(III) to form solid particles of MnO_2.
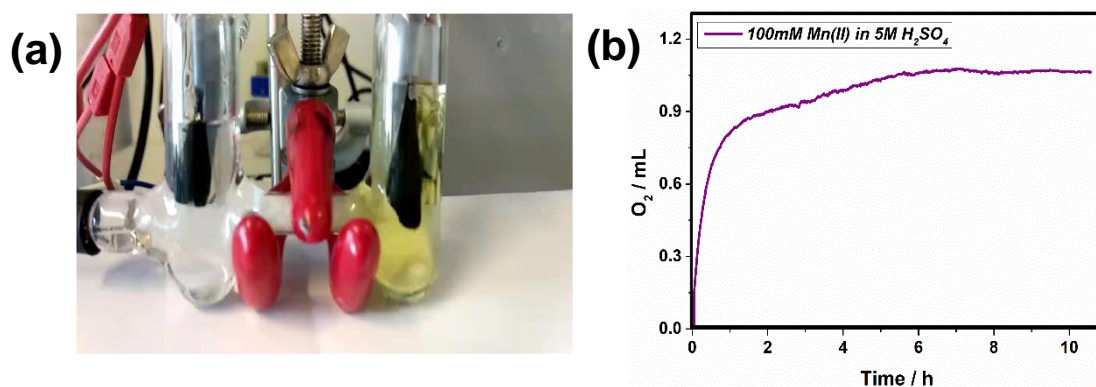

Figure 4.13 (a) H-cell setup (b) Pressure evolution chemical discharge of Mn(III) electrolyte with 50mg IrO_2 catalyst.

Conclusion and prespective:

Mn(II)/Mn(III) redox couple was investigated as an alternative to utilize at the positive side of the dual circuit redox flow battery. The Mn(II)/Mn(III) reaction proceeds through an ECE mechanism *i.e.* a reversible electrochemical oxidation of Mn(II) to Mn(III) followed by an irreversible chemical reaction of Mn(III) intermediates with the solvent to form $MnO_2(s)$ and Mn(II). The disproportionation reaction of Mn(III) was countered using TiO^{2+} and VO_2^+ ions. It was understood that there is a reduction in the platting of MnO_2 with the addition of the TiO^{2+} ions in the Mn(II) electrolyte. With the presence of VO_2^+ ions in the Mn and Mn-Ti electrolyte there was a significant decrease in the plating as compared to Mn-Ti electrolyte only, which was further confirmed by SEM analysis. Rotating disk study suggested that the reaction kinetics is limited due to the disproportionation of Mn(III) not by mass transport from the bulk to the electrode. Further, it also provided an insight for the two step oxidation process *i.e.* Mn(II) to Mn(III) at 1.54 V whereas Mn(II) to Mn(IV), at 2.01 V, followed by the oxygen evolution at above 2.3 V *vs.* SHE. The RRDE experiment didn't prove to be favourable as the collection efficiency obtained with all the four electrolytes was quite low. The chemically discharge OER test on IrO_2 catalyst with charged Mn(III) electrolyte displayed oxygen evolution. However, due to the disproportionation of Mn(III), the efficiency was quite low. From future prespective, OER will be investigated with the rest three electrolytes and in order to quantify the disproportionation of Mn(III) and examine the formation of complex if any, between all the three redox species, and spectroelectrochemistry analysis will be performed.

Bibliography:

[1] Larcher, D.; Tarascon, J. M. Towards Greener and More Sustainable Batteries for Electrical Energy Storage. *Nat. Chem.* **2015**, 7 (1), 19–29.

[2] Whittingham, M. History, Evolution, and Future Status of Energy Storage, Proceedings of the IEEE, Vol. 100, **2012**, 1518 – 1534.

[3]Hadjipaschalis, I.; Poullikkas, A.; Efthimiou, V. Overview of current and future energy storage technologies for electric power applications, *Renewable and Sustainable Energy Reviews*, Volume 13, **2009**,1513-1522

[4] Winter, M.; Brodd, R. J. What Are Batteries, Fuel Cells, and Supercapacitors? *Chem. Rev.* **2004**, 104 (10), 4245–4269.

[5] Batteries and Fuel Cells Chemistry - BC Open Textbooks, (https://opentextbc.ca/chemistry/chapter/17-5-batteries-and-fuel-cells)

[6] (http://glencoe.mheducation.com/sites/007874637x/student_view0/chapt er20/ section 2/self_check_quizzes.html#quest4

[7] https://www.extremetech.com/extreme/212388-accidental- nanoparticles-could-let-lithium-ion-batteries-live-another-day)

[8] Nitta, N.; Wu, F.; Lee, J.;Yushin, G. Li-ion battery materials: present and future, *Materials today*, Volume 18, **2015**, 252-264.

[9] Linden's Handbook of Batteries, Fourth Edition (https://www.accessengineeringlibrary.com/.../lindens-handbook-of-batteries-fourth-ed.)

[10] Berndt, D. Maintenance-free batteries : lead-acid, nickel/cadmium, nickel/metal hydride. A handbook of battery technology; 2. ed.. United Kingdom: N. p., **1997**.

[11] Blurton, K.; Sammells, A. Metal/air batteries: Their status and potential, *Journal of Power Sources*, 4 (**1979**) 263 – 279.

[12] Liang, X.; Hart, C.; Pang, Q.; Garsuch, A.; Weiss, T. and Nazar, L. F.; A highly efficient polysulfide mediator for lithium-sulfur batteries, *Nat. Commun.*, **2015**, 6, 5682.

[13] Dunn, B., Kamath, H. & Tarascon. *Science,* 334, 928–935 (**2011**).

[14] Thaller L. H.US Patent N 3,996,064 : *Electrically rechargeable redox flow cell*, **1976**.

[15] Posner A. *Fuel*, **1955**, 34, 330–338.

[16] Jan B. *Redox Fuel Cell*, US Patent N 3,540,933 :**1970**.

[17] Pan F.; Wang Q. Redox Species of Redox Flow Batteries: A Review, *Molecules*, **2015**, 20, 20499-20517.

[18] Bartolozzi M. Development of redox flow batteries - A historical bibliography, *J. Power Sources*, **1989**, 27, 219–234.

[19] Ponce de Leon C.; Frias-Ferrer A.; Gonzalez-Garcia J.; Szanto D.; Walsh F. Redox flow cells for energy conversion, *J. Power Sources*, **2006**, 160, 716–732.

[20] Skyllas-Kazacos, M.; Chakrabarti, M. H.; Hajimolana, S. A.; Mjalli, F. S.; Saleem, M. Progress in Flow Battery Research and Development, *J. Electrochem. Soc.*, **2011**, 158, R55–79.

[21] Savinell, R. F.; Tutorial at Paul Scherrer Institute, Villigen: "Overview of redox flow battery at NASA", **2012**.

[22] Aaron, D.; Liu, Q.; Tang, Z.; Grim, G.; Papandrew, A.; Turhan, A.; Zawodzinski T. A.; Mench, M. Dramatic performance gains in vanadium redox flow batteries through modified cell architecture. *J. Power Sources*, **2012**, 206, 450–453.

[23] Yue, L.; Li, W.; Sun, F.; Zhao, L.; Xing, L. Highly hydroxylated carbon fibres as electrode materials of all-vanadium redox flow battery. *Carbon*, **2010**, 48, 3079–3090.

[24] Friedrich, J. M.; Ponce-de-Leo´n, C.; Reade, G. W.; Walsh, F. C. Reticulated vitreous carbon as an electrode material. *J. Electroanal. Chem.*; **2004**, 561, 203–217.

[25] Rychcik M.; Skyllas-Kazacos, M. Evaluation of electrode materials for vanadium redox cell. *Journal of Power Sources*. **1987**, 19, 45 – 54.

[26] Li, W.; Liu, J.; Yan, C. Multi-walled carbon nanotubes used as an electrode reaction catalyst for VO2+/VO2+ for a vanadium redox flow battery. *Carbon*, **2011**, 49.

[27] Arora, P.; Zhang, Z.; Battery separators. *Chem. Rev.*, **2004**, 104, 4419–4462.

[28] Li, X.; Zhang, H.; Mai, Z.; Zhang H.; Vankelecom, I. Ion exchange membranes for vanadium redox flow battery (VRB) applications. *Energy & Environmental Science*, **2011**, 4, 1147.

[29] Prifti, H.; Parasuraman, A.; Winardi, S.; Lim, T. M.; Skyllas-Kazacos, M. Membranes for redox flow battery applications. *Membranes,* **2012**, 2(2), 275-306.

[30] Xi, J.; Wu, Z.; Qiu, X.; Chen, L. Nafion/SiO2 hybrid membrane for vanadium redox flow battery. *Journal of Power Sources*, **2007**, 166, 531–536.

[31] Schwenzer, B.; Zhang, J.; Kim, S.; Li, L.; Liu, J.; Yang, Z. Membrane development for vanadium redox flow batteries. *ChemSusChem*, **2011**, 4, 1388–1406.

[32] Mohammadi, T.; Chieng, S. C.; Skyllas Kazacos, M. Water transport study across commercial ion exchange membranes in the vanadium redox flow battery. *Journal of Membrane Science*, 133 (**1997**) 151-159.

[33] Qiua, J.; Zhaia, M.; Chenb, J.; Wanga, Y.; Penga, J.; Xua, L.; Lia, J. Genshuan Weia. Performance of vanadium redox flow battery with a novel amphoteric ion exchange membrane synthesized by two-step grafting method. *Journal of Membrane Science*, Volume 342, **2009**, 215-220.

[34] Sum, E.; Rychcik, M.; Skyllas-Kazacos, M. Investigation of the V(V)/V(IV) system for use in the positive half-cell of a redox battery. *J. Power Sources*, **1985**, 16, 85–95.

[35] Thaller, L. *Redox flow cell energy storage systems*. In Proceedings of the Terrestrial Energy Systems Conference, Orlando, FL, USA, 4–6 June 1979; American Institute of Aeronautics and Astronautics: New York, NY, USA, **1979**.

[36] Fang, B.; Iwasa, S.; Wei, Y.; Arai, T.; Kumagai, M. A study of the Ce (III)/Ce (IV) redox couple for redox flow battery application. *Electrochim. Acta*, **2002**, 47, 3971–3976.

[37] Xue, F.-Q.; Wang, Y.-L.; Wang, W.-H.; Wang, X.-D. Investigation on the electrode process of the Mn(II)/Mn(III) couple in redox flow battery. *Electrochim. Acta,* **2008**, 53, 6636–6642.

[38] Zhou, H.; Zhang, H.; Zhao, P.; Yi, B. A comparative study of carbon felt and activated carbon based electrodes for sodium polysulfide/bromine redox flow battery. *Electrochim. Acta*, **2006**, 51, 6304–6312.

[39] Wang, Y.; Lin, M.; Wan, C. A study of the discharge performance of the Ti/Fe redox flow system. *Journal of power sources*, **1984**, 13, 65–74.

[40] Lim, H.; Lackner, A.; Knechtli, R. Zinc-bromine secondary battery. *J. Electrochem. Soc.*, **1977**, 124, 1154–1157.

[41] Tang, C.; Zhou, D. Methanesulfonic acid solution as supporting electrolyte for zinc-vanadium redox battery. *Electrochim. Acta,* **2012**, 65, 179–184.

[42] Leung, P.; Ponce de Leo´n, C.; Walsh, F. An undivided zinc–cerium redox flow battery operating at room temperature. *Electrochem. Commun*, **2011**, 13, 770–773.

[43] Skyllas-Kazacos, M. Novel vanadium chloride/polyhalide redox flow battery. *J. Power Sources*, **2003**, 124, 299–302.

[44] Wang, W.; Li, L.; Nie, Z.; Chen, B.; Luo, Q.; Shao, Y.; Wei, X.; Chen, F.; Xia, G.; Yang, Z. A new hybrid redox flow battery with multiple redox couples. *Journal of Power Sources*, 216 (**2012**) 99-103.

[45] Li, X.; Hao, X.; Abudulaa, A.; Guan, G. Nanostructured catalysts for electrochemical watersplitting: current state and prospects. *J. Mater. Chem. A*, **2016**, 4, 11973.

[46] Bockris, J.; Conway, B.; Yeager, E. Comprehensive Treatise of Electrochemistry. Volume 2: *Electrochemical Processing*. New York: Plenum Press, **1981**.

[47] Godwin, I.; Rovetta, A.; Lyons, M.; Coleman, J. *Electrochemical water oxidation: The next five years*, Current Opinion in Electrochemistry. **2018**, 7, 31–35.

[48] Carmo, M.; Fritz, D.; Mergel, J.; Stolten, D. A comprehensive review on PEM water electrolysis. *Int. J. Hydrogen Energy*, **2013**, 38, 4901–4934.

[49] Matsumoto, Y.; Sato, E. Electrocatalytic properties of transition metal oxides for oxygen evolution reaction. *Materials Chemistry and Physics*, I4 (**1986**) 397-426.

[50] Trotochaud, L.; Ranney, J.; Williams, K.; Boettcher, S. Solution-cast metal oxide thin film electrocatalysts for oxygen evolution. *J. Am. Chem. Soc.*, **2012**, 134, 17253–17261.

[51] Morita, M.; Iwakura, C.; Tamura, H. The anodic characteristics of massive manganese oxide electrode. *Electrochim. Acta*, 24 (**1979**) 357.

[52] Amstutz, V.; Toghill, K.; Powlesland, F.; Vrubel, H.; Comninellis, C.; Hu, X.; Girault, H. Renewable hydrogen generation from a dual-circuit redox flow battery. *Energy Environ. Sci.*, **2014**, 7, 2350.

[53] Amstutz, V.; Toghill, K.; Comninellis, C.; Girault, H. EOS Holding (Switzerland), International Pat., WO 2013131838, **2013**.

[54] Davies, G. *Coordin. Chem. Rev.*, 4, 199 (**1969**).

[55] Fleischmann, M.; Thirsk, H. R.; and Tordesillas, I. M. *Trans. Faraday Soc.* 58 (**1962**).

[56] Kao, W. H.; Weibel. Electrochemical oxidation of manganese(II) at a platinum electrode. *Journal of Applied Electrochemistry*, 22 (**1992**) 21-27.

[57] Cartwright, A.; and Paul, R. L. 'Manganese Dioxide Symposium', Vol. 2, Tokyo (**1980**) p. 290.

[58] Paul, R. L.; and Cartwright, A. *J. Electroanal. Chem.* 201 (**1986**) 113.

[59] Clarke, C. J.; Browning, G. J.; Donne, S. W. An RDE and RRDE study into the electrodeposition of manganese dioxide. *Electrochimica Acta*, 51 (**2006**) 5773–5784.

[60] Lee, H. J.; Park, S.; Kim, H. Analysis of the Effect of MnO2 Precipitation on the Performance of a V/Mn Redox Flow Battery. *Journal of the Electrochemical Society*, 165 (5) (**2018**) A952-A956.

[61] Dong, Y.; Kaku, H.; Hanafusa, K.; Moriuchi, K.; Shigematsu, T. A novel titanium/manganese redox flow battery. *ECS Transactions*, 69 (18) 59-67 (**2015**).

[62] Bard, A. J.; Faulkner, L. R. Electrochemical Methods. Fundamentals and Applications. New York: Wiley, **2001**.

[63] (https://www.slideshare.net/AfrinNirfa1/cyclic-voltammetry)

[64] https://www.pineresearch.com/shop/knowledgebase/rotating-electrode-theory

[65] Levich, V. G. Physicochemical Hydrodynamics, Prentice-Hall, Upper Saddle River NJ (**1962**).

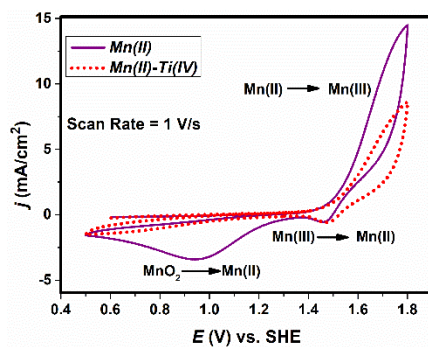[66] Albery, W. J.; Hitchman, M. L. Ring-Disc Electrodes, *Clarendon Press*, Oxford (**1971**).

Figure 1.1 CV 0.1M Mn(II) and 0.1M Mn(II)-Ti(IV) in 5M H_2SO_4. Conditions: working electrode: glassy carbon. Scan rate = 1 V/s.
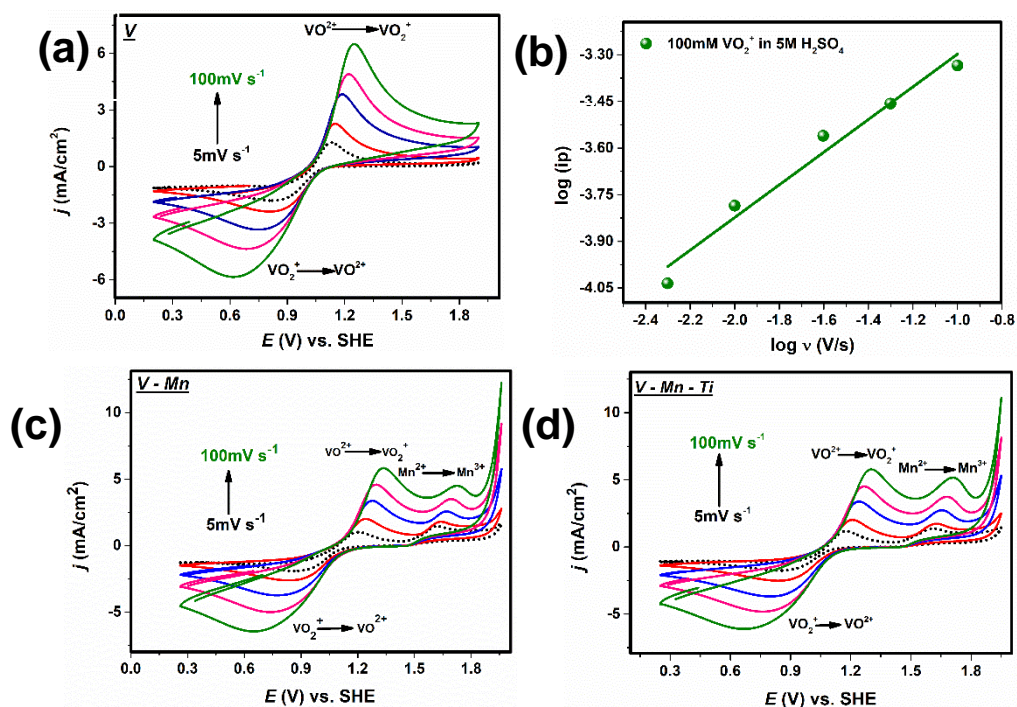

Figure 1.2 a) Scan rate dependence with (a) VO_2^+ (b) plot of log (scan rate) vs. log(peak current) for VO_2^+ (c) VO_2^+- Mn(II) (d) VO_2^+- Mn(II) – Ti(IV) in 5M H_2SO_4.
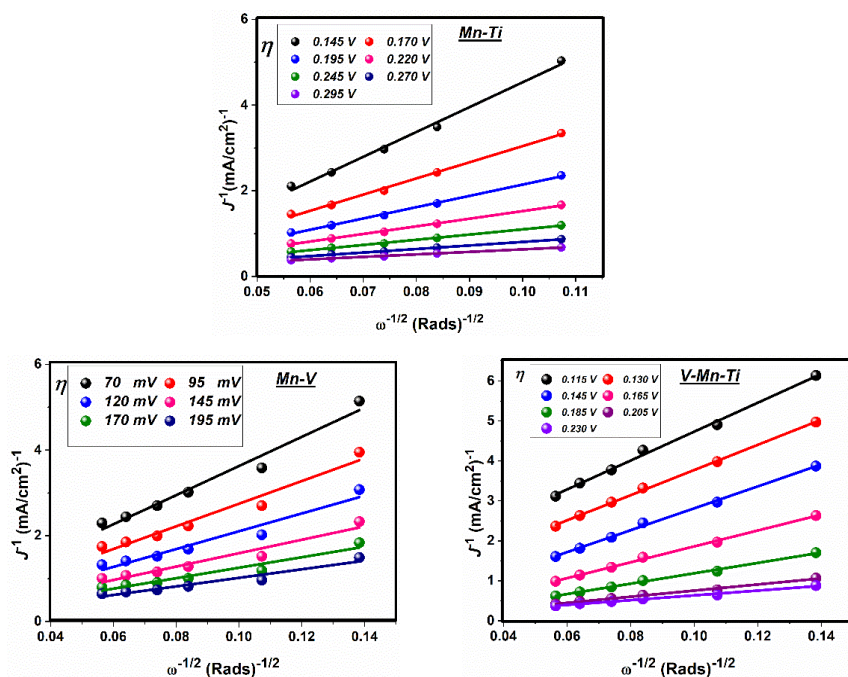
Figure 1.3 a) Koutecky Levich plots obtained from 0.1 Mn(II), 0.1M Mn(II)-Ti(IV), 0.1M Mn(II)-Ti(IV)-V(V).
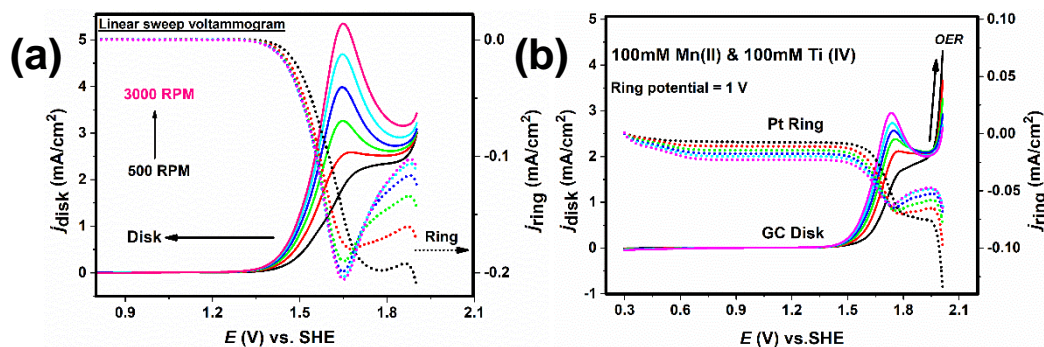

Figure 1.4 a) RRDE of (a) 0.1 Mn(II) (b) 0.1M Mn(II)-Ti(IV) in 5M H_2SO_4. Conditions: scan rate: 10mV/s

The theoretical collection efficiency (N) for the RRDE setup was calculated using the solved equations for diffusion-convection published by W. J. Albery [60-62]. The collection efficiency of RRDE depends on the disk, ring geometry, and is independent of rotation speed, conc. of analyte etc. Table 1, shows the various calculated parameters required and the final expression required for the calculation of collection efficiency:

$$\beta^{2/3} = (r^3_3 - r^3_2 / r_1^3), \alpha = (r_2 / r_1)^3 - 1$$

α	0.520875
β	0.676125
r_2/r_1	1.15

r_3/r_2	1.1304
$F(\alpha)$	0.5975
$F(\alpha/\beta)$	0.6544
$F[(\alpha/)(\alpha + \beta)]$	0.24
α / β	0.770383
$(\alpha /\beta)(1+ \alpha + \beta)$	1.692531
$1/(\alpha/\beta)(1+\alpha+\beta)$	0.590831

Table 1.6. Parameters extracted from the ring-disk geometry for theoretical collection efficiency.

$$N = 1 - F\left(\frac{\alpha}{\beta}\right) + \beta^{\frac{2}{3}}[1 - F(\alpha)] - (1 + \alpha + \beta)^{\frac{2}{3}}\left\{1 - F\left[\left(\frac{\alpha}{\beta}\right)(1 + \alpha + \beta)\right]\right\}$$

The values for F(α) and F(β) were taken from the computed values for a particular ring-disk ratio (Ref). Substituting the values in the above expression displayed N = 0.2535.
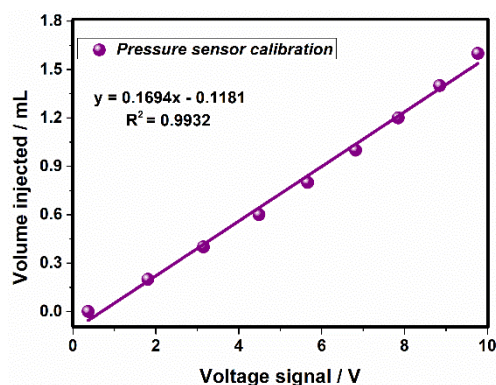

Figure 1.5: Pressure sensor calibration curve.